

# EXHAUST PLUME CONTAMINANTS FROM AN AGED HYDRAZINE

## MONOPROPELLANT THRUSTER

T. D. McCay, D. P. Weaver, W. D. Williams, H. M. Powell,

and J. W. L. Lewis

ARO, Inc.

AEDC Division

A Sverdrup Corporation Company

Arnold Air Force Station, Tennessee

### ABSTRACT

An experimental study of the exhaust plume of an aged (200,000 pulses) 0.44 N hydrazine monopropellant thruster has been performed with the goal of characterizing both the gas dynamic and contamination properties of the exhaust. The thruster was operated over a thrust range of 0.44 to 1.10 N with a nominal 0.14 sec on/10.0 sec off duty cycle using initial catalyst bed (Shell 405) temperatures of 367, 478 and 589 K. Exhaust diagnostic systems employed included a mass spectrometer probe, a quartz crystal microbalance (QCM), a laser-Raman/Rayleigh system, an electron beam which permitted fluorescence measurements and flow visualization, and a particle collector. Plume species number densities and rotational temperatures were determined along with mass deposition rates at various QCM cryogenic surface temperatures. Traditional engine performance para-

meters were also determined in order to relate performance and exhaust properties. This paper concentrates on contamination measurements made using the mass spectrometer probe and QCM. The results show the variation of species mole fractions and deposition rates with pulse number and operating condition along with the associated engine performance values. A significant increase in hydrazine concentrations in the plume was observed to occur at a point in time without significant loss of engine performance. This phenomenon was investigated in detail and the results are discussed.

## 1.0 INTRODUCTION

The use of monopropellant thrusters as attitude control systems and for station keeping functions has stimulated interest over the past several years in the contamination characteristics of their plume exhausts. The tendency for present-day satellites and spacecraft is to have a large number of cryogenic temperature surfaces, one effect of which increases the importance of knowing the types and quantities of possible contaminating elements in the propulsion devices' exhausts. The contamination characteristics of a thruster include the mass flux of particulate, condensate and raw fuel, for both the forward-flow and back-flow regions of the exhaust; and the applications of such knowledge are obvious. This particular study has concentrated its investigations in the forward-flow region and had as its goal the measurements of not only the contaminant mass flux but also the gas dynamic properties of the plume exhaust to verify and quantitatively determine the relationship between the gas dynamic properties and the contamination level and nature of its source.

To accomplish these tasks use was made of an aged monopropellant hydrazine engine of nominal 0.44 N thrust level which was operated in the pulsed mode. In addition to the usual engine properties of combustion chamber pressure, catalyst bed wall temperature and fuel mass flow rate, measurements were performed to determine the gas dynamic properties (species densities and temperature) at both the engine exit plane and in the forward-flow expansion region, the contaminant mass flux, and the nature of the solid and/or liquid particulate in the exhaust. Particular emphasis was placed on the detection and identification of catalyst-bed particles.

This paper presents a description of the experimental techniques employed to accomplish these goals, exemplary gas dynamic data and a detailed presentation of the contaminant measurements obtained using the mass spectrometer probe and QCM. Additionally, a description of a catastrophic increase in plume contaminants that occurred during the thruster study will be presented along with a documentation of thruster performance changes after this occurrence. A total of 18 test periods of two days duration each were necessary to complete the experimental study.

## 2.0 EXPERIMENTAL APPARATUS AND PROCEDURES

### 2.1 Thruster

The thruster studied is a single injector monopropellant hydrazine device which contains Shell 405 catalyst material. The thruster is designed to provide 0.44 N thrust and a specific impulse of 2099 N-sec/kg at a steady-state chamber pressure of  $5.93 \times 10^5$  Pa. The exhaust was provided by a conical nozzle with 0.76 mm throat diameter and an exit area ratio of 55. Prior to the measurements of the exhaust properties,

engine performance levels were determined by measuring the thruster combustion chamber pressure and fuel mass flow rate for several values of valve inlet pressure. The results compare well with previous measurements performed by the engine manufacturer, as well as previous investigators.<sup>1</sup>

The prepulse catalyst bed temperature was systematically varied over the range of 366.5 to 477.6 K using an external heater, and fuel temperature was nominally room temperature (285 K). The external lower wall temperature of the combustion chamber and the nozzle throat temperature were measured throughout this work. Chemical analysis of the hydrazine fuel was performed to determine its chemical purity, and all specifications were satisfied (Mil-P-26536C). The engine was operated in a pulsed mode, and the chamber pressure was varied from 5.86 to  $14.1 \times 10^5$  Pa. The pulse width, as determined from engine solenoid valve current traces, was nominally 140 msec. A schematic of the thruster is shown as Fig. 1. The radiation heat shield shown in the figure was removed prior to operating the thruster at AEDC.

## 2.2 Vacuum Chamber

The engine was contained within a cryogenically-pumped research vacuum chamber with a diameter and length of 1.2 m and 5.2 m, respectively. Liquid  $N_2$ , gaseous He at 20 K and liquid He were used for cryogenic pumping of the plume exhaust products, and for the highest engine thrust condition studied the chamber background pressure was less than

---

<sup>1</sup>Baerwald, R. K. and Passamaneck, R. S., Monopropellant Thruster Exhaust Plume Contamination Measurements, AFRPL-TR-77-44 (1977).

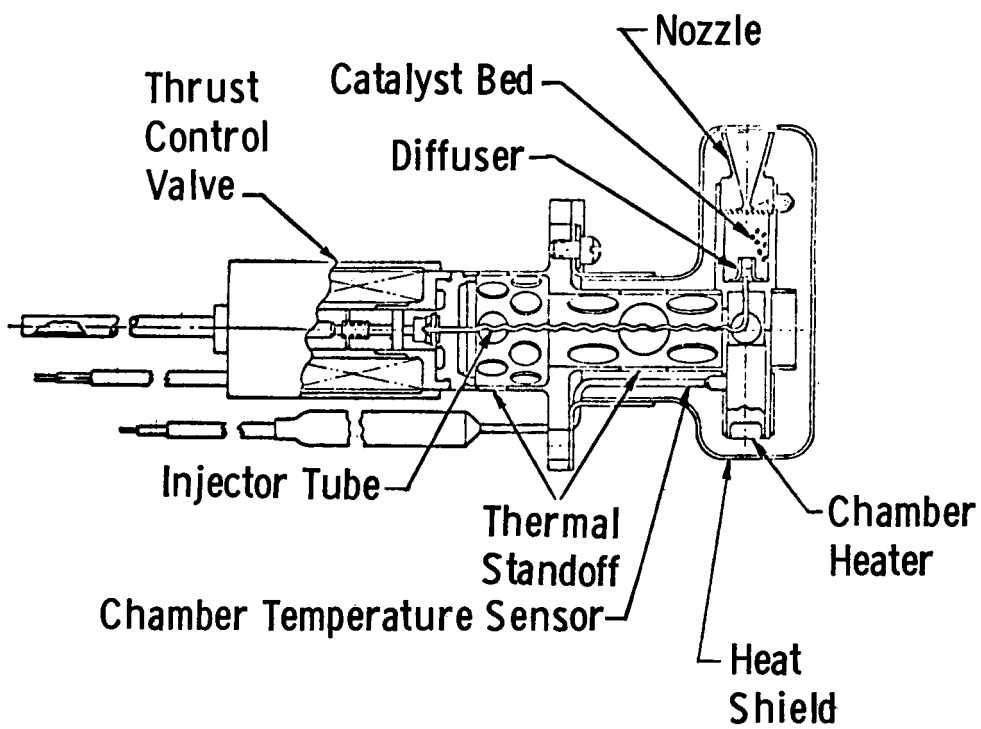


**Fig. 1 0.1-lbf-Thrust Monopropellant Engine**

$9.3 \times 10^{-2}$  Pa, corresponding to a simulated altitude of approximately 94 km. The engine was mounted on a traversing mechanism with three linear degrees of freedom which allowed all flowfield instrumentation to be stationary; Fig. 2 shows the location of the engine within the vacuum chamber. A description of the vacuum chamber and thruster is contained in a previous paper.<sup>2</sup>

### 2.3 Mass Spectrometer Probe

The cryogenically pumped mass spectrometer probe used in this investigation has been described in detail in a previous publication<sup>3</sup>. The gaseous helium-cooled probe, shown in Fig. 3, was located on the thrust axis and centerline of the thruster plume with the skimmer tip located at axial positions  $450 \leq \hat{x} \leq 650$ . The probe was fabricated in two thermally-insulated sections; the front section was cooled to 12-20 K for pumping purposes, and the aft section, containing the electronics, was uncooled. Since the 12 K probe temperature would not cryopump (adsorb) the plume hydrogen, CO<sub>2</sub> was periodically injected into the probe to permit H<sub>2</sub> pumping by absorption into the resultant CO<sub>2</sub> frost.

The probe functions under the same principle as a molecular beam system. In effect, the probe serves as the last stage of a two-stage miniature molecular beam-mass spectrometer system. For free jets (plumes exhausting to vacuum) with little condensation, this gives practically an

---

<sup>2</sup>Williams, W. D., McCay, T. D., Powell, H. M., Weaver, D. P., Price, L. L. and Lewis, J. W. L., Experimental Study of Monopropellant Hydrazine Thruster Exhaust. JANNAF 10th Plume Technology Meeting, San Diego, CA. (1977).

<sup>3</sup>McCay, T. D., Powell, H. M. and Busby, M. R., Direct Mass Spectrometric Measurements in a Highly Expanded Rocket Exhaust Plume, AIAA Paper 77-154 (1977).

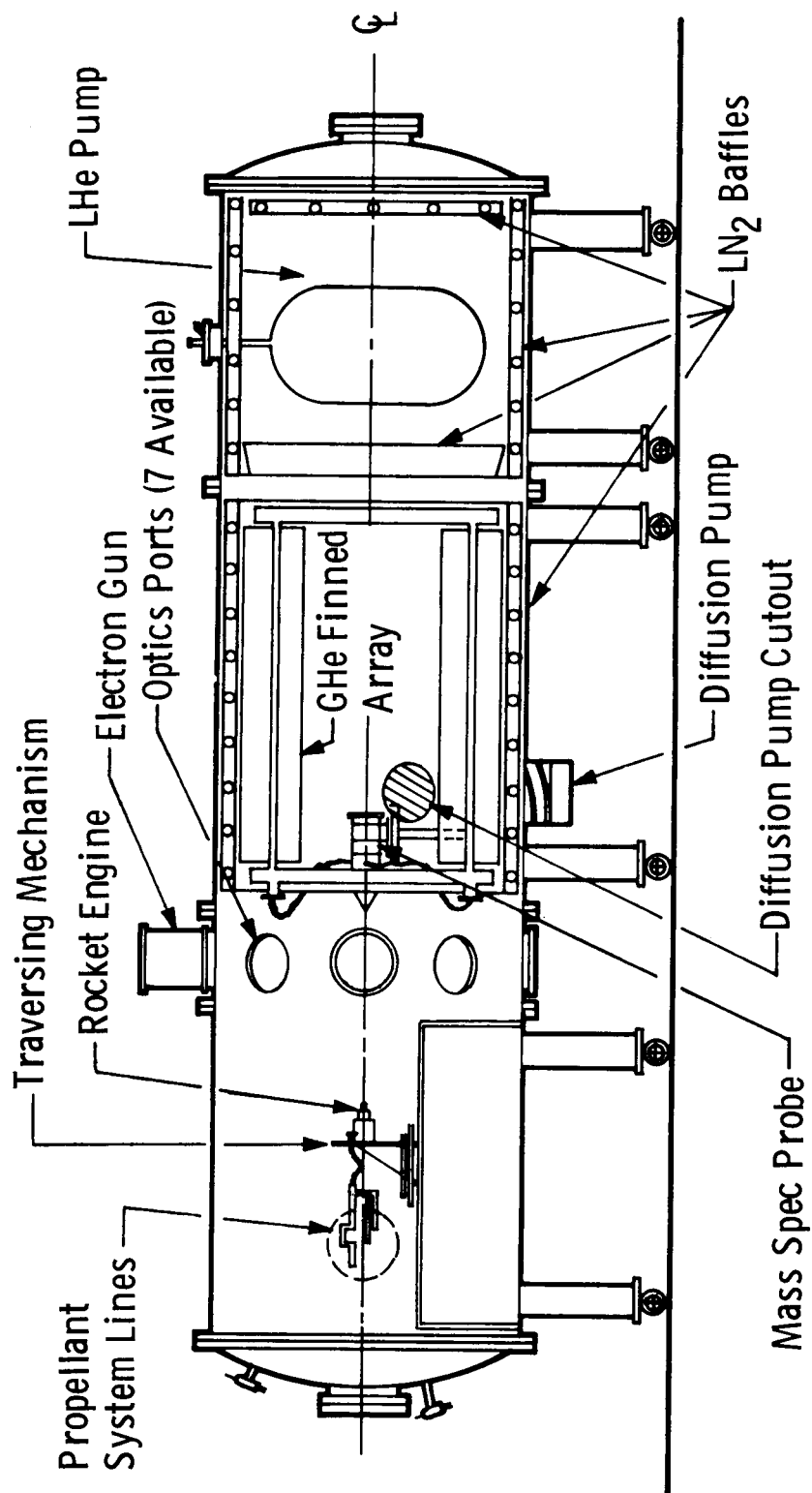


Fig. 2 Engine Installation in 4- by 10-ft Chamber

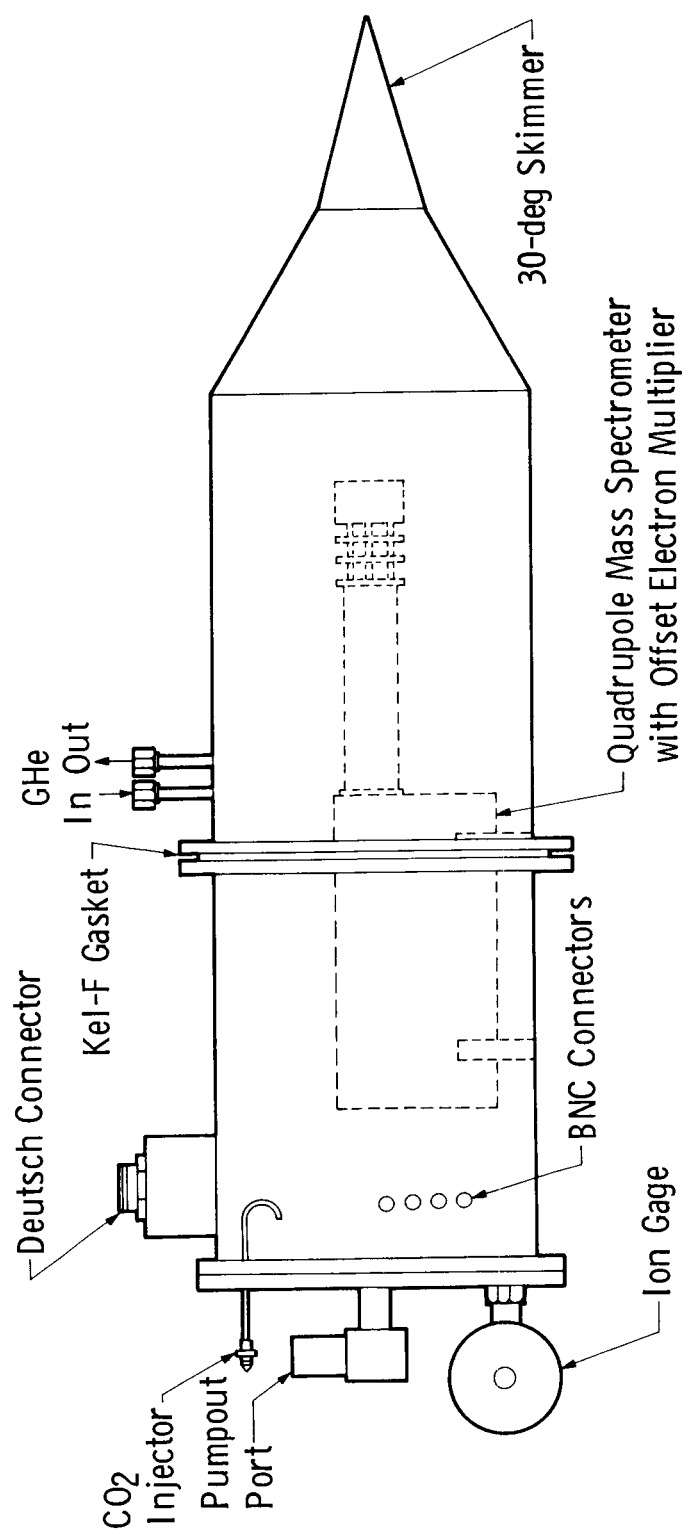


Fig. 3 Schematic of Mass Spectrometer Probe



unperturbed measurement of jet species. Basic operation consists of the probe skimming a molecular beam from the plume centerline which is directed onto the ion source entrance aperture that serves as a collimator. Only a small fraction of the entering gases is ionized in the ion source, with the remainder passing through the quadrupole section and paraxial multiplier and impinging upon the probe endplate.

The mass spectrometer data were taken in two basic modes, either the spectrometer was swept over the entire 0-55 atomic mass unit (amu) mass range as many times as possible during the engine pulse, or a limited sweep was employed which swept over a four-amu mass range and permitted detailed intrapulse data to be obtained for that range. Data were output on a Visicorder<sup>®</sup> oscillograph. The data obtained were for the primary species of interest,  $H_2$ ,  $NH_3$ ,  $H_2O$ ,  $N_2$  and  $N_2H_4$ ; mole fraction rather than absolute number density measurements were made. From previous investigations<sup>4</sup> it has been determined that published values<sup>5</sup> for ionization cross sections and cracking patterns were applicable for the quadrupole system used in the probe. Therefore, these were employed in reduction of the mass spectrometer data.

## 2.4 The Quartz Crystal Microbalance System

A quartz crystal microbalance (QCM) was utilized in this study for measurements of the mass deposition rate and total mass deposition in the exhaust plume. Measurements were made for crystal surface temperatures

<sup>4</sup>McCay, T. D., Powell, H. M. and Busby, M. R., Development of a Cryogenically Pumped Mass Spectrometer Probe for Rocket Plume Studies, AEDC-TR-76-55.

<sup>5</sup>Cornu, A. and Massot, R., Compilation of Mass Spectral Data, 2nd ed., Vol. I, Heydon, New York (1975).

in the range 90 to 200 K at a variety of radial and axial positions in the forward flow region of the thruster for a wide range of engine operating conditions.

The QCM consists of a quartz crystal, an electronic oscillator, and a data processing/recording system. The piezoelectric effect of the quartz crystal is used to stabilize the resonance frequency of the oscillator. This resonance frequency, which depends upon the angle of the crystal cut, is found to be a function of the mass deposited on the crystal surface and the crystal surface temperature. The relation for the change in frequency,  $\Delta f$ , that results when the crystal experiences a mass change,  $\Delta M$ , and temperature change,  $\Delta T$ , is given by

$$\Delta f = C_m \Delta M + C_T \Delta T \quad (1)$$

where  $C_m$  is the mass coefficient and  $C_T$  is the temperature coefficient of the quartz crystal.

Since a measurement of the variation of QCM frequency with deposited mass was required, care was taken to minimize the influence of temperature on the observed frequency. For this reason a QCM of the temperature compensating variety developed by JPL<sup>1</sup> was utilized. For this type of QCM a doublet crystal is cut and electrodes suitably arranged such that two independent crystal oscillators are obtained. For the two crystals,

$$\Delta f_1 = C_{m_1} \Delta M_1 + C_{T_1} \Delta T_2 \quad \text{and} \quad \Delta f_2 = C_{m_2} \Delta M_2 + C_{T_2} \Delta T_2 . \quad (2)$$

Since two crystals are of identical piezoelectric properties and are constrained to identical temperature environments,

$$C_{m_1} = C_{m_2}, C_{T_1} = C_{T_2}, \text{ and } \Delta T_1 = \Delta T_2,$$

and the following relation results:

$$\Delta f = \Delta f_1 - \Delta f_2 = C_{m_1} (\Delta M_1 - \Delta M_2) \quad (3)$$

When one of the crystal surfaces is shielded from mass deposition, the beat frequency shift of the two crystals is given by the following simple relation:

$$\Delta f = C_{m_1} \Delta M_1 \quad (4)$$

An evaluation of the mass coefficient,  $C_m$ , yields the desired mass deposition rate expression utilized for this study:

$$\frac{dM}{dt} = 1.524 \times 10^{-8} \frac{df}{dt} \quad (5)$$

where the mass deposition rate per unit area,  $dM/dt$ , is given in grams/cm<sup>2</sup>-sec when  $df/dt$  is given in Hz/sec.

The QCM utilized in this study was supplied by the Jet Propulsion Laboratory and had an AT crystal cut of 35°10'. This cut, which gives

a small temperature coefficient in the temperature range 125 K and above, when coupled with the JPL doublet crystal design, provides effective temperature compensation in the range over which measurements were made.

The QCM unit was cooled by thermal contact via a metal conduction path attached to the 4 x 10 chamber gaseous helium supply system. Resistance heaters, controlled by the thermocouple at the crystal surface, maintained the unit operating temperature. The ability to vary the crystal surface temperature allowed a gross distinction of the contaminating species. Expected condensate for a given QCM temperature is listed in Table 1 for reference.

<u>Table 1 Expected QCM Condensate</u>	
<u>QCM Temperature</u>	<u>Expected Condensate</u>
200 K	Trace Impurities
172 K	Hydrazine
144 K	Hydrazine and water
100 K	Hydrazine, water, ammonia

The experimental configuration of the QCM system for the two phases of the thruster study is depicted in Fig. 4. In test phase I, the QCM crystal surface was located at an angle of 30 deg relative to the chamber centerline and 38.75 cm from the center of the thruster exit plane for the thruster axis centered on the chamber centerline and the thruster cart in the forward-most position. For test phase II, the QCM crystal surface was positioned on the (thruster) chamber centerline at a distance of 113.35

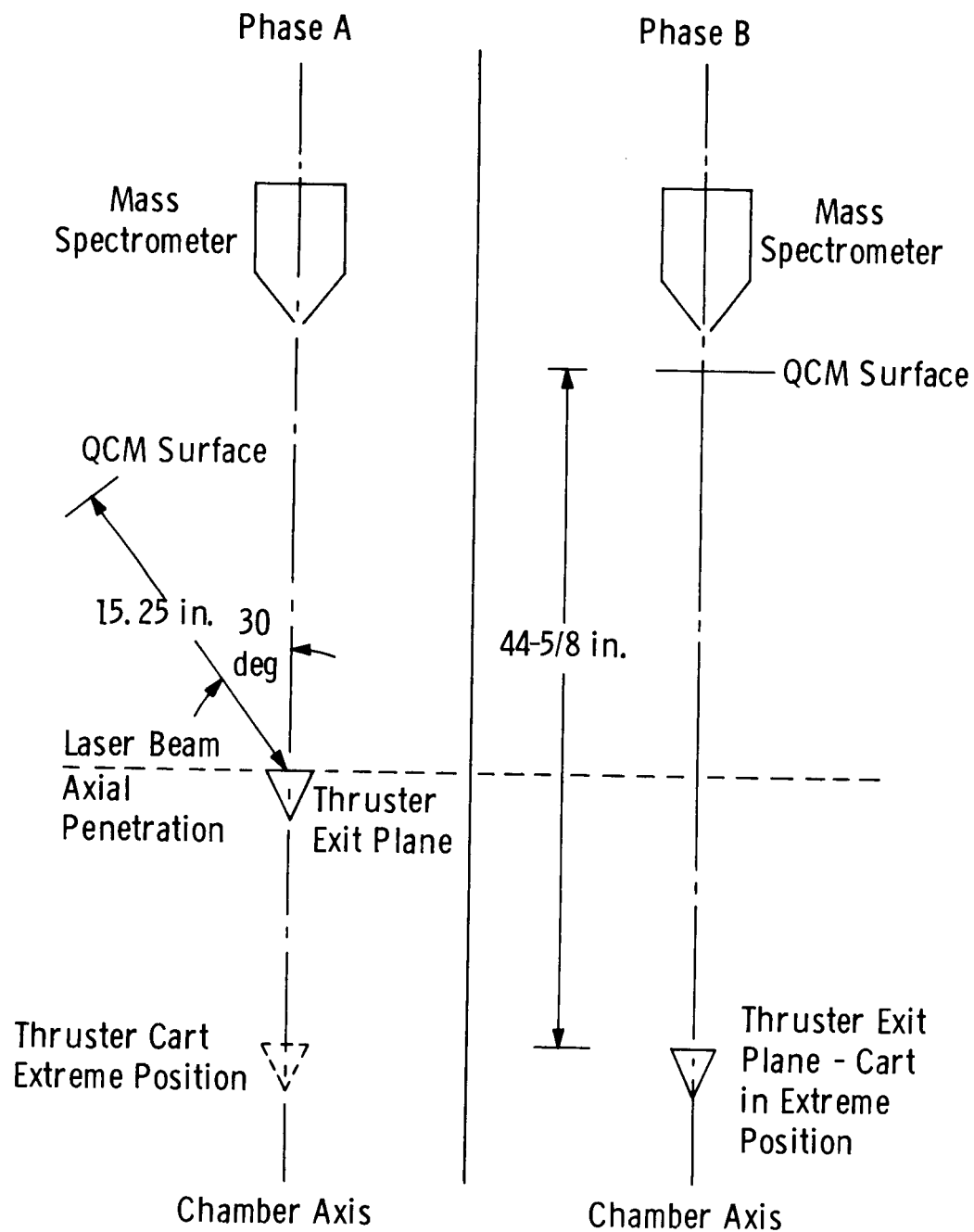


Fig. 4 QCM-Mass Spectrometer Configuration for Test Phase A and B

cm from the thruster exit plane with the thruster cart in the forward most position. For both experimental configurations, QCM position and surface angle with respect to the thruster exit plane was referenced in terms of an axial position from thruster exit and a radial distance perpendicular to the thruster axial centerline.

## 2.5 Laser Raman and Rayleigh/Mie System

Raman scattering<sup>6</sup> measurements were performed 0.5 and 1.3 cm downstream from the engine exit plane to determine the species number densities of  $N_2$ ,  $NH_3$  and  $H_2$  and the rotational temperature ( $T_R$ ) of  $H_2$ , which, because of sufficiently high gas density, is equal to the gas kinetic temperature. Such data were acquired for combustion chamber pressures covering the range 5.86 to  $14.1 \times 10^5$  Pa. A Holobeam 600 series pulsed ruby laser system was utilized to provide excitation for the Raman and Rayleigh/Mie scattering. The 6 x 3/8-inch ruby rod was oriented to provide a horizontally polarized beam, and the laser was operated in the conventional mode which provided a pulse width of 1 ms and an energy of 35 J per pulse at  $6943 \text{ \AA}$ . The laser beam energy was injected into the chamber via appropriate focusing optics, and the observed cylindrical focal volume, which was located on the thruster axial centerline, had the approximate dimensions of 1 mm diameter by 2.77 mm length. Figure 5 shows the experimental configuration for the Raman and Rayleigh/Mie systems as well as that for the electron beam system described in 2.6. A partial, synthetic spectrum for Raman scattering from a simulated plume exhaust is shown in Fig. 6. This spectrum

---

<sup>6</sup>Lewis, J. W. L. and Williams, W. D., Measurement of Temperature and Number Density in Hypersonic Flow Fields Using Laser Raman Spectroscopy, AIAA Paper No. 75-175, presented at the 13th AIAA Aerospace Sciences Meeting, Pasadena, CA, Jan. 20-22, 1975.



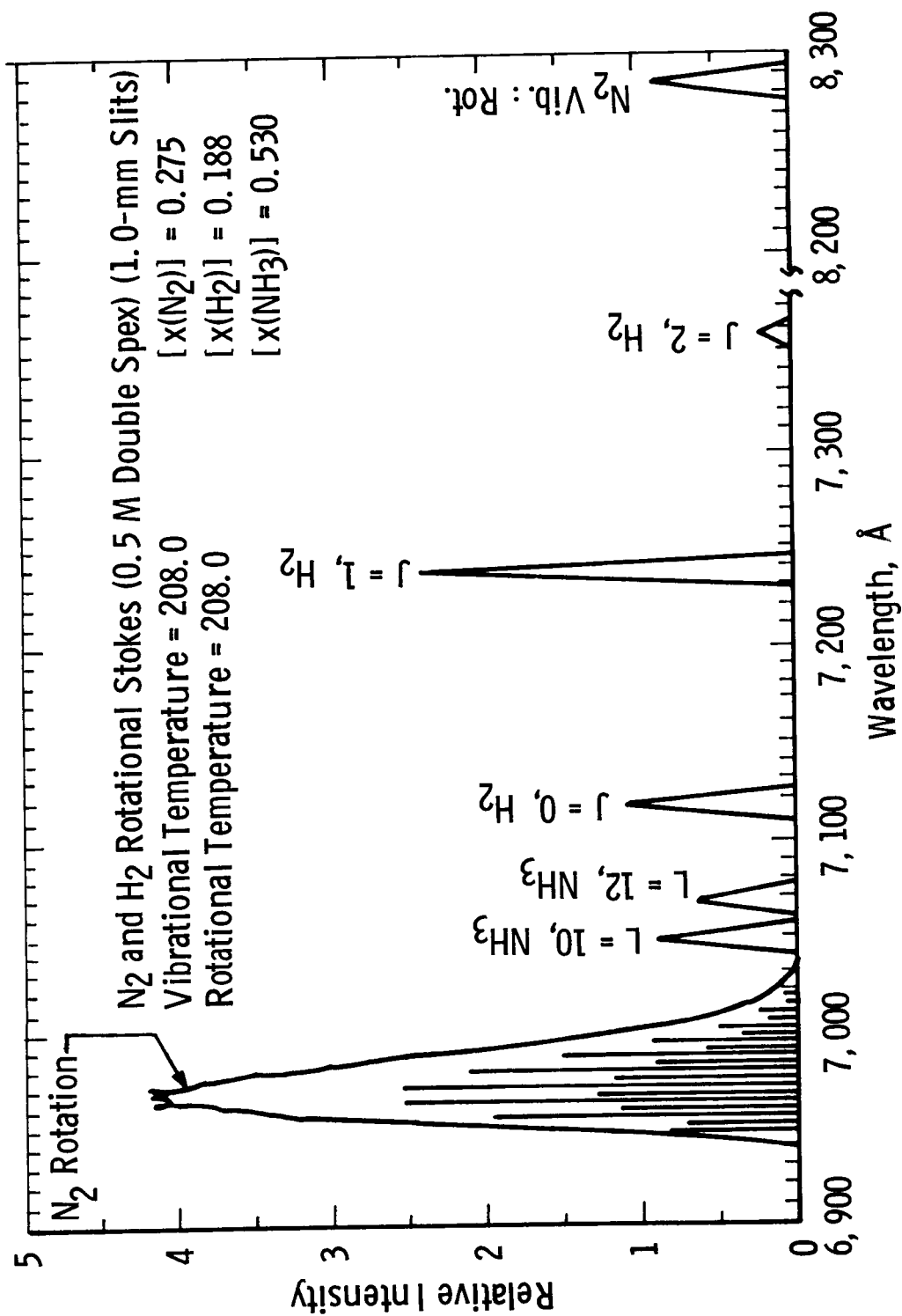


Fig. 6 Raman Scattering Synthetic Spectrum



is appropriate for the use of a 0.5-m focal length double spectrometer for spectral dispersion, and such a system with the necessary collection optics was used for these measurements and is shown in Fig. 5. All Raman data were Stokes Raman scattering signals, as seen in Fig. 6, and  $T_R$  was determined from the ratio of the  $J = 1$  and  $J = 0$   $H_2$  signals assuming metastable equilibrium for the nuclear spin states of ortho- and para- $H_2$ . The species number densities were obtained from individual rotational Raman lines or, in the case of  $N_2$ , from the vibration-rotation band, and in situ calibrations were performed to determine the system sensitivity. The data were acquired during a 1 msec period which occurred approximately 90 msec following opening of the engine valve and approximately 50 msec prior to valve closing. Data were acquired using a cooled photomultiplier tube (PMT) and routine photon detection systems. Data processing and initial analysis were performed using an on-line PDP-8 minicomputer system with line printer output. This data processing system was used for essentially all flow-field measurement systems.

Rayleigh (or Mie) scattering<sup>7</sup> data were acquired using the same laser system but with a filtered PMT detector channel, and the purpose of such data was to observe the presence of particulate or condensate within the plume exhaust. Rayleigh/Mie data were acquired over the same engine operation condition range as the Raman measurements and also for a range of catalyst bed temperatures and, further, the centerline spatial

---

<sup>7</sup>Lewis, J. W. L. and Williams, W. D. Argon Condensation in Free-Jet Expansions, AEDC-TR-74-32, July 1974.

region investigated was  $20 \leq \hat{x} \leq 300$ . During a subsequent experimental investigation a calibration will be performed to determine the scattering signal level from only the gaseous species in the plume exhaust, and the existence of particulate or condensate will be inferred.

## 2.6 Electron Beam System

For the flowfield expansion region for which the species density is too low to permit the use of Raman scattering, the electron beam fluorescence technique<sup>8</sup> was used to measure local values of  $N_2$  number density,  $n(N_2)$ , and rotational temperature ( $T_R$ ). The axial distance region investigated was  $78 \leq \hat{x} \leq 300$ , and at selected axial points, radial profiles of both  $n(N_2)$  and  $T_R$  were measured. To accomplish this, use was made of a 30 keV electron beam of approximately 1 mA beam current which was produced by an RCA model VC2126 V4 electron gun mounted in a stainless steel housing at the top of the chamber. The beam was injected into the chamber and flowfield through a 1.0-mm-diameter orifice and collected by a Faraday cup as shown in Fig. 5. Magnetic focusing provided a small diameter beam source at the centerline of the chamber, and the directing of the beam through the orifice was accomplished with an alignment yoke. Flow visualization capability was provided by a sweep-deflection coil located below the orifice and by associated control circuitry. The stationary beam could be deflected at any angle up to 30 degrees either side of vertical, or repetitively swept with a constant angular velocity through any angle and about any mean deflection angle.

No flow field perturbation is expected for the measurement of  $n(N_2)$

---

<sup>8</sup>Williams, W. D. , Hornkohl, J. O. and Lewis, J. W. L. Electron Beam Probe for a Low Density Hypersonic Wind Tunnel, AEDC-TR-71-61, July 1971.

and  $T_R$  by this technique. The  $N_2^+$  first negative fluorescent emission system and specifically the R-branch of the (0,1) vibrational band of this system was used for these measurements. The fluorescent radiation was collected by the 0.5-m spectrometer and processed by the detection and data acquisition systems.  $T_R$  was determined using the dipole excitation model and the usual Boltzmann analysis of the line intensities of the measured R-branch. Finally, data acquisition was accomplished during a 5 msec period located at the same temporal location of the Raman data.

## 2.7 Particle Collector

The sample collecting system shown in Fig. 7 consisted of two components, an aluminum housing and the collectors themselves. The housing was made of eight strips of one-inch-wide aluminum bolted and welded together to form a web with one open end. The collectors were standard scanning electron microscope (SEM) disks mounted to the housing and consisted of aluminum stubs with vacuum-deposited, copper-coated glass covers. The actual sampling surfaces were of three types; the bare copper itself; beeswax melted onto the copper surface; and SEM quality Microstick<sup>®</sup> glue dripped onto the copper substrate and spread by moving the disks to and fro. A total of 84 disks, 9 with wax, 16 with glue and 59 with bare copper were distributed throughout the aluminum web.

The sampling was carried out by installing the web in the vacuum chamber such that the engine nozzle exit was located in the center and in the plane of the open end of the web. The axis of the engine nozzle was located along the centerline of the web length. The engine

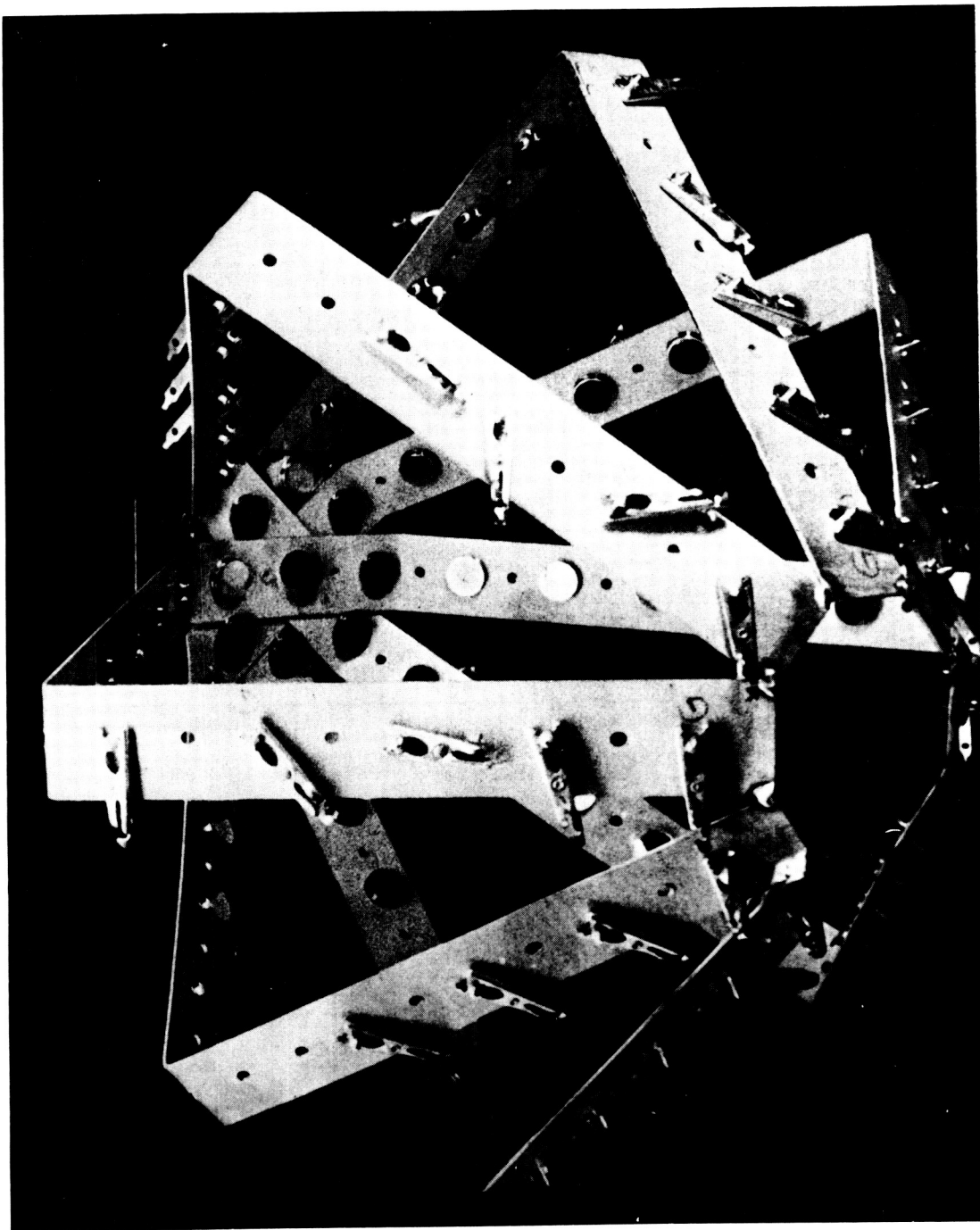


Fig. 7 Particle Collector

was pulsed into the web approximately 1000 times, and then the web was removed from the vacuum system. The SEM disks were removed and placed on stands in dust-free boxes from subsequent viewing with the SEM.

### 3.0 RESULTS AND DISCUSSION

The thruster was operated during 18 test periods over a duration of nine months. The thruster performance was determined prior to any exhaust measurements, during two interim test periods, and subsequent to the exhaust measurements. The basic operating conditions of the thruster and the nomenclature attached to each condition are shown in Table 2. Additional discussion of thruster performance is presented in a subsequent section of this paper.

Table 2 Thruster Test Conditions

Condition	Initial Catalyst Temp., K	Inlet Pressure Pa (psia)	Chamber Pressure Pa (psia)	Chamber Temp.
1A	367	$1.59 \times 10^6$ (230)	$9.31 \times 10^5$ (135)	665 K
1B	367	$2.04 \times 10^6$ (296)	$1.21 \times 10^6$ (175)	695 K
1C	367	$2.41 \times 10^6$ (349)	$1.41 \times 10^6$ (205)	715 K
2A	478	$1.58 \times 10^6$ (230)	$9.31 \times 10^5$ (135)	700 K
2B	478	$2.04 \times 10^6$ (296)	$1.21 \times 10^6$ (175)	730 K
2C	478	$2.41 \times 10^6$ (349)	$1.41 \times 10^6$ (205)	745 K
2S	478	$1.00 \times 10^6$ (145)	$5.86 \times 10^5$ (85)	650 K
3A	589	$1.59 \times 10^6$ (230)	$9.31 \times 10^5$ (135)	735 K
3B	589	$2.04 \times 10^6$ (296)	$1.21 \times 10^6$ (175)	760 K
3C	589	$2.41 \times 10^6$ (349)	$1.41 \times 10^6$ (205)	775 K

Duty cycle: 0.138 sec on/10.0 sec off as determined by valve opening and closing

### 3.1 Laser Raman, Rayleigh/Mie and Electron Beam Results

A summary of the Raman scattering data from a single test period is shown in Table 3 for the engine conditions investigated. The results show the absolute values of species number densities of  $N_2$ ,  $H_2$  and  $NH_3$  as well as  $T_R$  for the two axial positions for the various engine conditions. Also shown are the values of the sum ( $n_T$ ) of these number densities.

Table 3 Summary of Raman Measurements - Test Period No. 11

Condition	$\hat{x}$	$\frac{n(N_2)}{(cm^{-3})}$	$\frac{n(H_2)}{(cm^{-3})}$	$\frac{n(NH_3)}{(cm^{-3})}$	$\frac{n_T}{(cm^{-3})}$	$\frac{T_R}{(K)}$	$T_R/T_o$
2A	18.5	$4.9 \times 10^{16*}$	$5.5 \times 10^{16}$			183	0.26
2B	↓	$5.4 \times 10^{16}$	$6.8 \times 10^{16}$			148	0.20
2C		$7.2 \times 10^{16}$	$7.3 \times 10^{16}$			185	0.25
2S		$2.9 \times 10^{16}$	$3.6 \times 10^{16}$			177	0.27
2A	28.5	$2.3 \times 10^{16}$	$3.3 \times 10^{16}$	$2.4 \times 10^{16}$	$8.1 \times 10^{16}$	121	0.17
2B	↓	$2.2 \times 10^{16}$	$3.5 \times 10^{16}$	$3.8 \times 10^{16}$	$9.6 \times 10^{16}$	119	0.16
2C		$3.1 \times 10^{16}$	$3.8 \times 10^{16}$	$3.0 \times 10^{16}$	$9.9 \times 10^{16}$	106	0.14
2S		$1.4 \times 10^{16}$	$2.3 \times 10^{16}$			99	0.15

\*Average of test period No. 6 and 14 results.

Figure 8 shows the axial variation of the Rayleigh (or Mie) scattered signal for the engine conditions studied.

Shown in Fig. 9 as an exemplary result is an isodensity map for  $n(N_2)$  as determined by the electron beam technique, and Fig. 10 shows the radial profiles of  $n(N_2)$  at three axial positions. Both axial and radial profiles of not only  $n(N_2)$  but also  $T_R$  were obtained and will be published in a subsequent report.

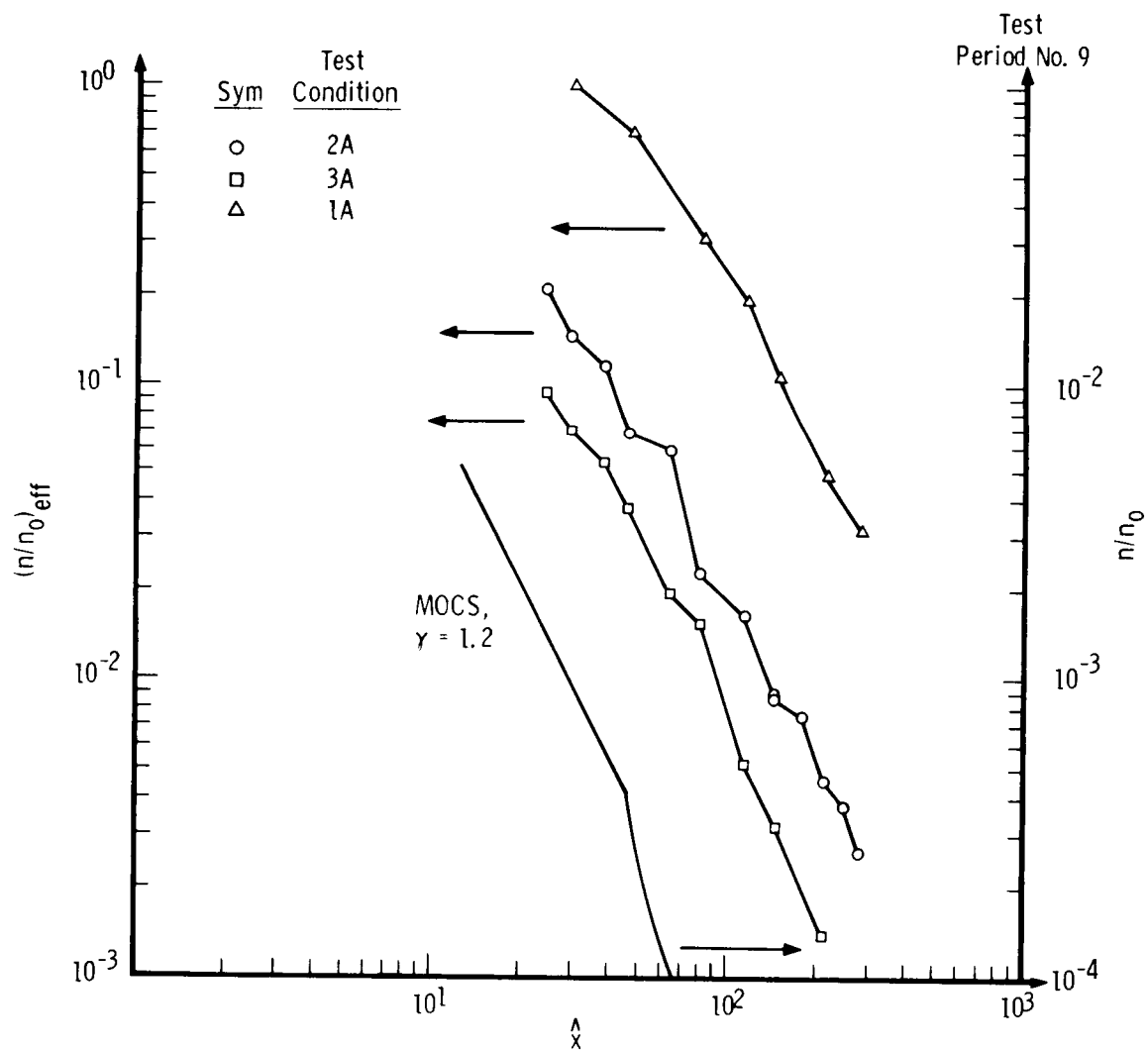


Fig. 8 Axial Variation of Rayleigh/MIE Scattering

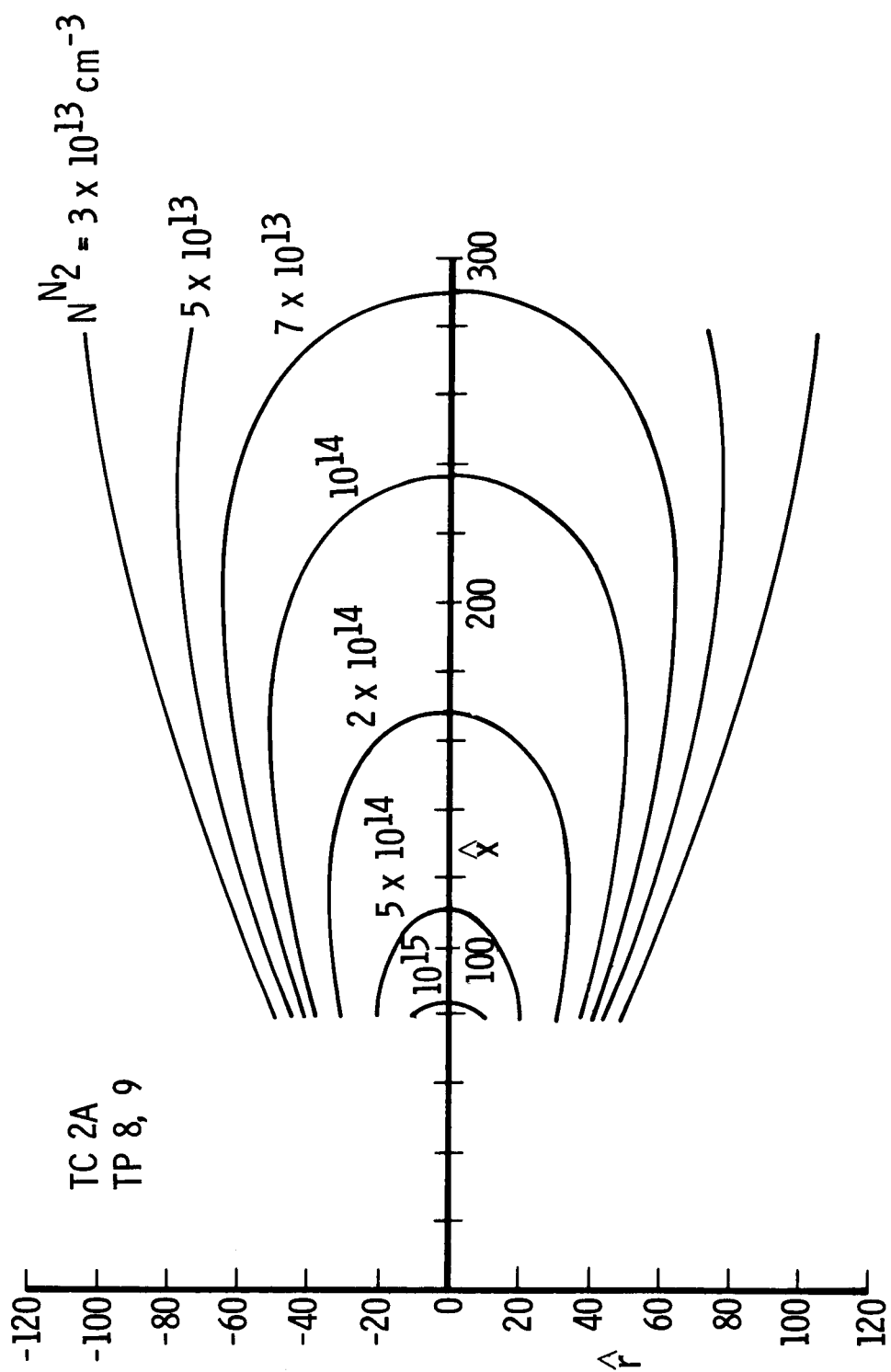


Fig. 9 Electron Beam  $N_2$  Isodensity Map from Radial Survey



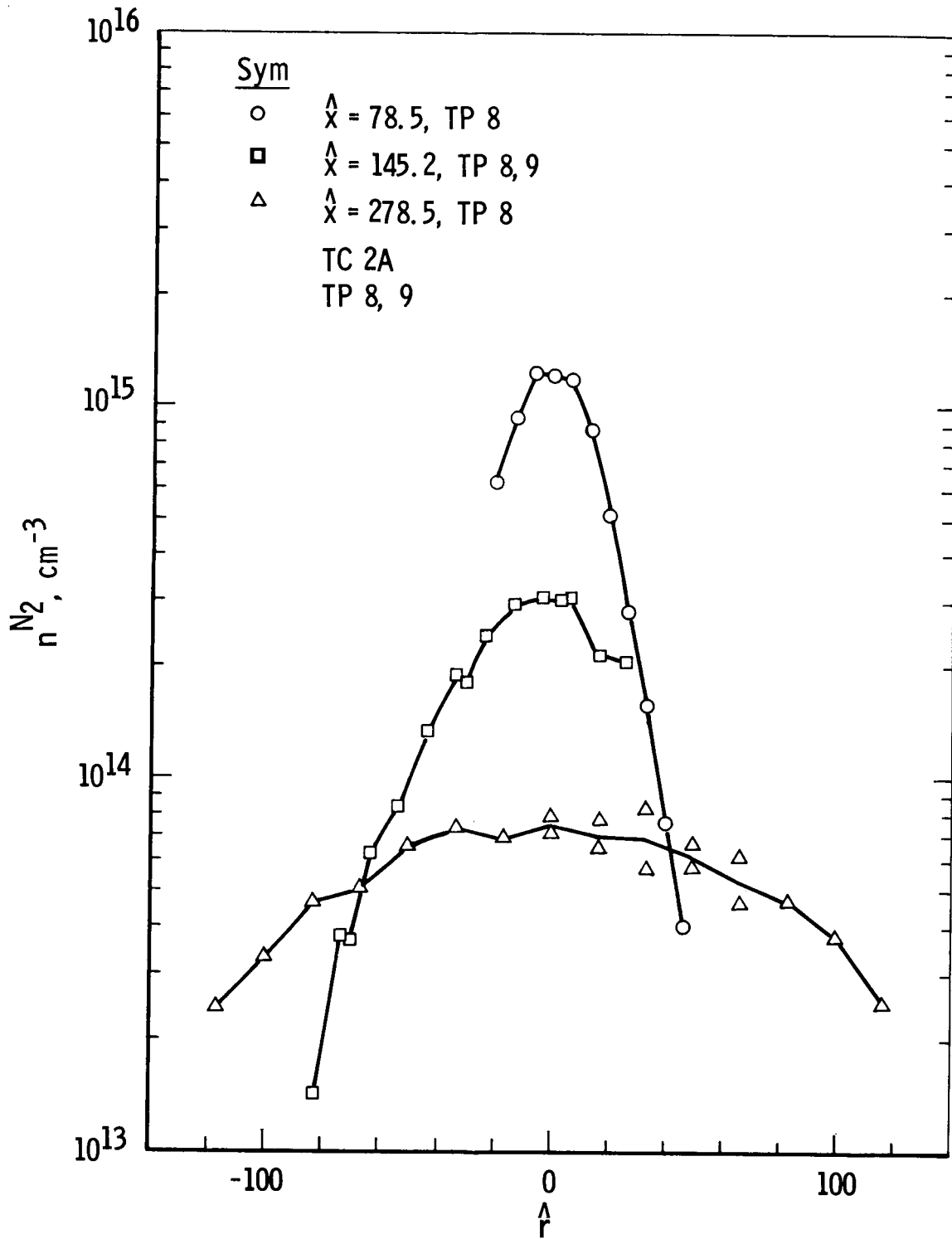


Fig. 10 Electron Beam Radial Survey of  $N_2$  Number Density

The axial variation of  $n(N_2)/n_o(N_2)$  is shown in Fig. 11, and it is to be noted that the Raman data represent an average of the last 20-25 pulses of a 30-pulse train. That these results are representative of the steady-state portion of the pulse train was verified by mass spectrometric and electron beam data. The values of  $n_o$  used for Fig. 11 are estimated to have an inaccuracy of  $\pm 10\%$ . A significant result shown by Fig. 11 is the discrepancy of the measured and predicted axial variations of  $n(N_2)$ . Further improvements in the boundary layer corrections are not expected to remove the discrepancy. This discrepancy can be attributed, at least in part, to an inaccurate composition and mixture specific heat ratio ( $\gamma$ ) used for the calculation. Similarly, the validity of the assumption of frozen chemistry, although most likely true for the freestream, is not certain for the region of flow interior to the nozzle. The possibility of vibrational relaxation of  $NH_3$ , which will also affect the value of  $\gamma$ , should also be included for accurate predictions. No conclusions can be offered at this time regarding the possibility of systematic variations in  $n(N_2)/n_o(N_2)$  with engine inlet pressure.

Conclusions similar to those for the axial variation of the species density values of  $n(N_2)/n_o(N_2)$  can be given for the axial variation of  $T_R/T_o$ , as shown in Fig. 12. Both electron beam and Raman data for a single test condition are shown in Fig 12, and while the Raman measurement at  $\hat{x} = 18.5$  is in good agreement with calculation, the discrepancy worsens with increasing  $\hat{x}$ . It is important to note that the temperature is lower than predicted, which will enhance the condensation of such species as  $NH_3$ .

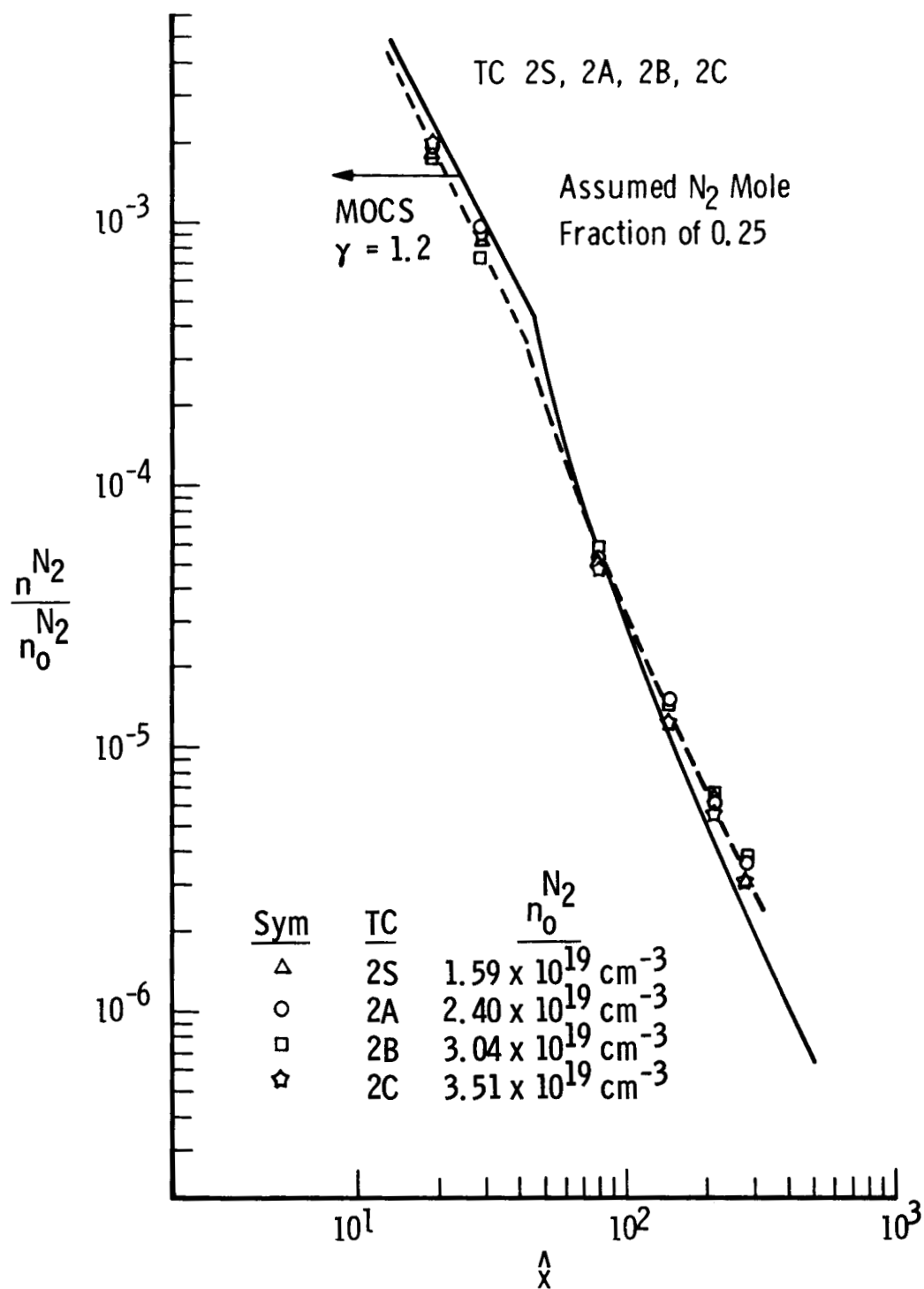


Fig. 11 Axial Survey of  $N_2$  Number Density

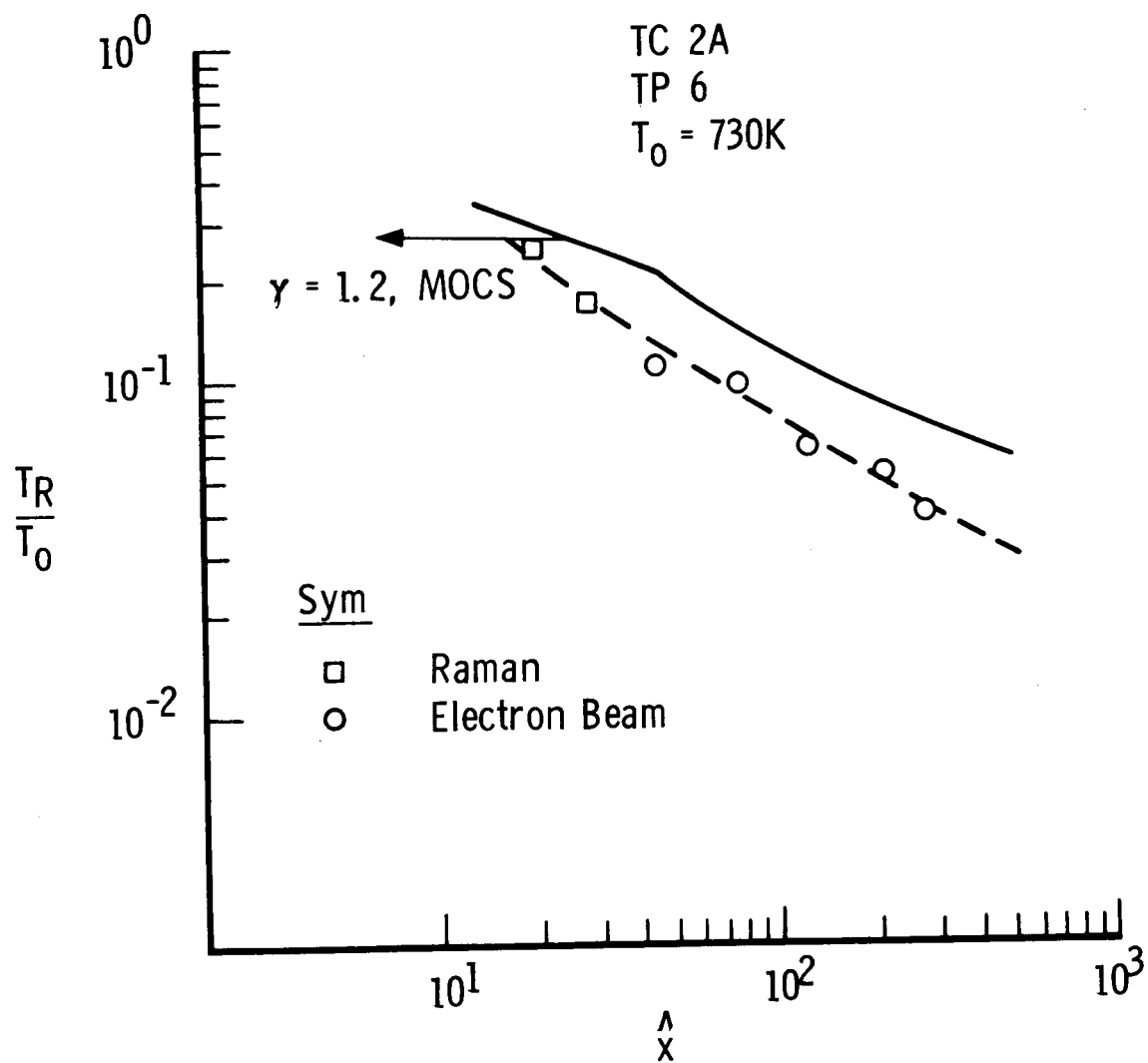


Fig. 12 Axial Survey of Rotational Temperature

Using the results of Figs. 11 and 12, one can compute and generate a graphical variation of the static pressure  $P$  with  $T_R$  (or  $T$ ) for the expansion. The result from Figs. 11 and 12 is shown in Fig. 13. From this figure it is seen that the isentropic relation  $PT^{\gamma/(1-\gamma)} = \text{constant}$  is obeyed, and a simple computation yields  $\gamma = 1.29$ . Thus, the previous assumption of frozen chemistry in the freestream is given quantitative support.

The Rayleigh/Mie scattering data shown in Fig. 8 were obtained for the purpose of determining the existence of condensate and/or catalyst bed particles. The data of Fig. 8 for an approximately constant chamber pressure ( $P_c$ ) of  $9.31 \times 10^5$  Pa show an order of magnitude increase in scattering as the catalyst bed temperature is decreased from 589 to 367 K. Quite possibly liquid fuel is being observed. Furthermore, for a catalyst bed temperature of 478 K, the scattering signal has been observed to increase with an increase in  $n_0$ ; as  $n_0$  increased by a factor of approximately 1.4, the absolute scattering signal increased by a factor of approximately 1.6, which may possibly be the result of condensation of  $\text{NH}_3$ . To clarify these observations, further analysis and calibrations are required and are in progress.

## 3.2 Mass Spectrometer Results

### 3.2.1 Ammonia/Nitrogen Ratios

The ratio of ammonia to nitrogen mole fractions was monitored throughout the test periods in which the mass spectrometer was installed and operating. Tabulated results which are averaged over test periods 6-11

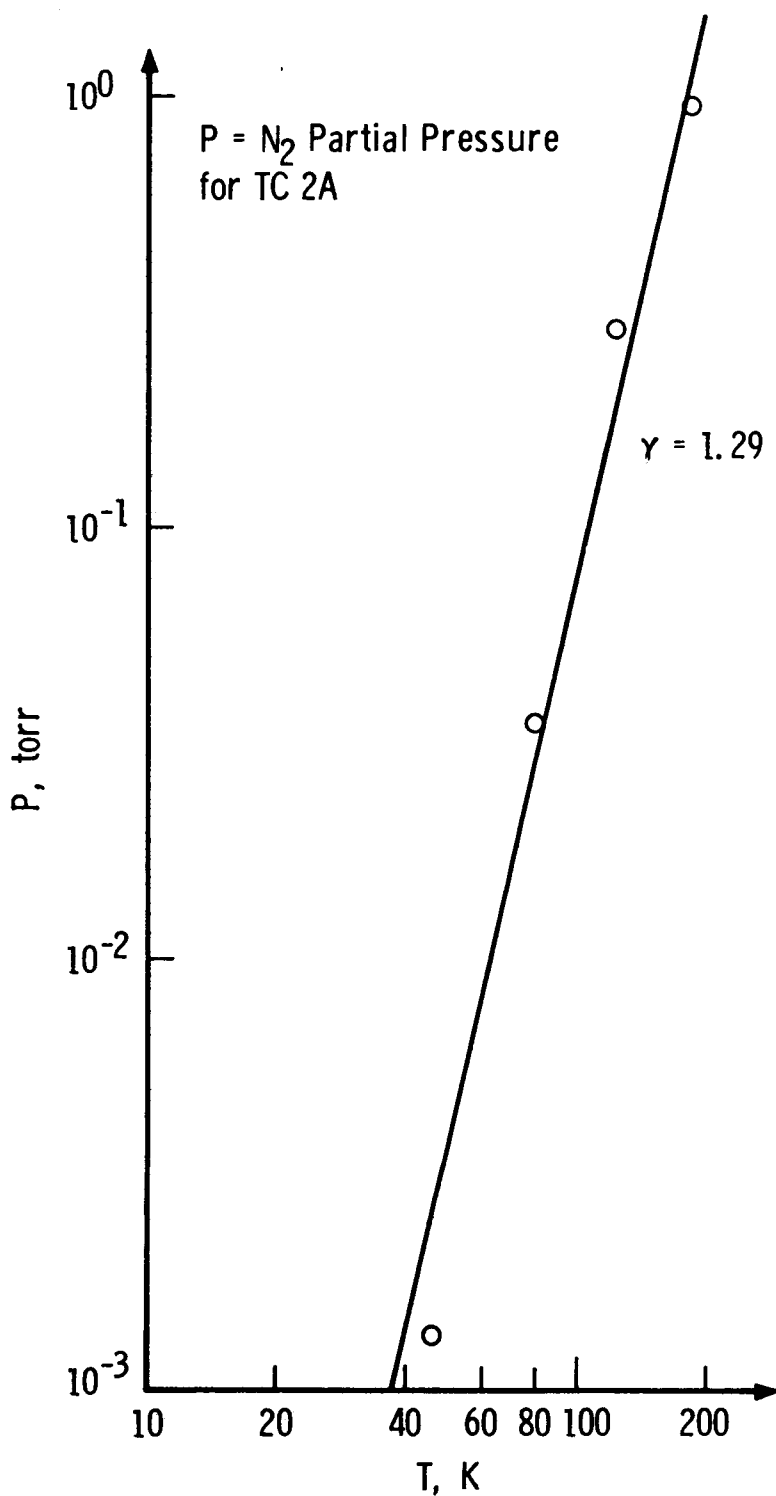


Fig. 13 Pressure-Temperature Variation

are shown in Table 4. The results are indicative of increasing ammonia dissociation with pulse number (due to thruster heating). The first pulse data show an inconsistency due to the large concentrations of hydrazine and general inconsistent behavior of the thruster during first pulses.

Table 4 Far Field Ammonia to Nitrogen Mole Fraction Ratios  
(Mass Spectrometer Data)

Pulse Number	Thruster Test Condition								Avg.
	2S	1A	2A	3A	1B	2B	3B	2C	
1	3.40	3.42	3.58	3.10	3.43	2.64	2.97	3.35	3.24
5	2.08	2.36	2.17	1.72	2.57	2.21	2.03	2.43	2.20
10	1.94	1.93	1.91	1.58	1.90	1.80	1.64	1.66	1.80
15	2.02	1.77	1.82	1.74	1.91	1.73	1.64	1.65	1.79
25	1.82	1.58	1.78	1.61	1.65	1.64	1.63	1.73	1.68

The ratios can be employed to give equilibrium ammonia dissociation levels by employing the equation

$$\frac{[\text{NH}_3]}{[\text{N}_2]_{\text{equilibrium}}} = \frac{4(1-x)}{(1+2x)} \quad (6)$$

where  $x$  = ammonia dissociation fraction. Table 5 gives the dissociation fraction assuming equilibrium dissociation and the average pulse values given in Table 4.

Table 5 Equilibrium Values of Ammonia Dissociation Fractions - Mass Spectrometer Results

Pulse Number	$[\text{NH}_3]/[\text{N}_2]$	Corresponding Equilibrium $x$
1	3.24	0.072
5	2.20	0.214
10	1.80	0.289
15	1.79	0.292
25	1.68	0.299

The intrapulse variation of ammonia to nitrogen was not monitored in general; however, limited data were taken in anticipation of possible future interest. The results for pulses 11-25 (average) for test condition 2A are shown in Fig. 14. These results are consistent with the data in Table 4 which were taken at 0.090 sec into the pulse to correspond to the laser and electron beam data gate.

Due to the lack of detailed calibration data for the mass spectrometer system and the large variations due to engine (and possibly spectrometer) fluctuations, no good evaluation of the error in the mass spectrometer measurements can be offered. A cursory analysis does indicate that the variations in species ratios are within 20%.

### 3.2.2 Species Variation with Pulse Number

During the mass spectrometer testing periods the five species of primary interest ( $\text{N}_2$ ,  $\text{NH}_3$ ,  $\text{H}_2\text{O}$ ,  $\text{N}_2$  and  $\text{N}_2\text{H}_4$ ) were monitored as functions of pulse number for several test conditions. These types of data were employed in determination of the ammonia to nitrogen ratios



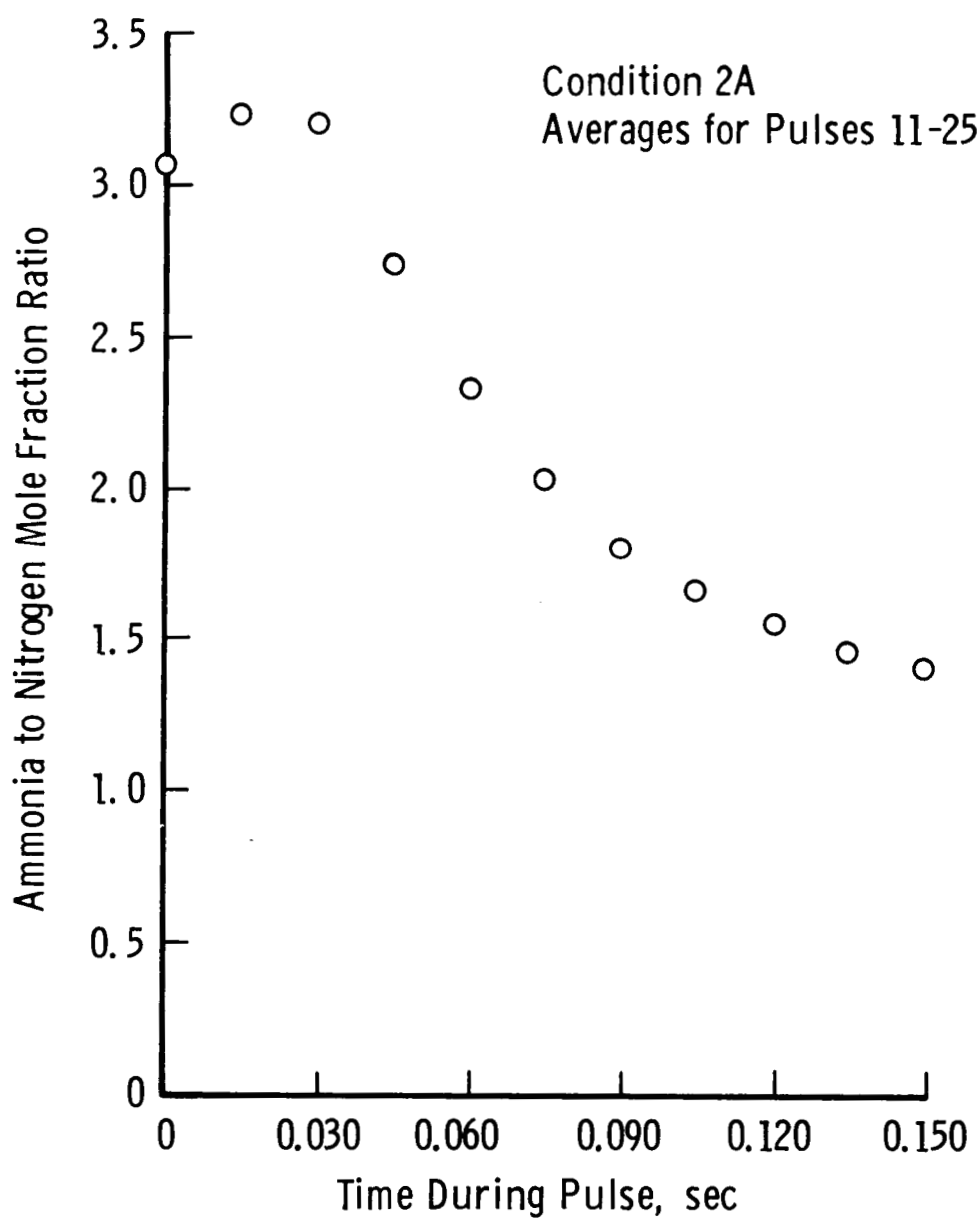


Fig. 14 Variation of Mole Fraction Ratio  $[\text{NH}_3/\text{N}_2]$  within the Pulse

presented in the previous section. In most instances, all of these species were monitored, but in several instances the hydrogen peak signal to noise ratio was quite poor, and the hydrogen data could not be used. This high background noise was associated with the large quantities of  $H_2$  absorbed into the  $CO_2$  frost used for pumping in the probe. In addition, ammonia and hydrazine contributed daughter peaks of mass 2 which significantly degraded hydrogen data quality.

Several cases for which five species data were obtained are presented in this section as mole fraction data. Mole fractions for each species for conditions 2A, 2B and 2C are shown in Figs. 15, 16 and 17, respectively. The most noteworthy of the species' properties are the large mole fractions of  $N_2H_4$  present during pulse one of each case and the small number of pulses necessary to reduce the  $N_2H_4$  value significantly. Ammonia to nitrogen ratios for these cases may not necessarily agree with those from the previous section, since these are individual runs and the previous section data represented averaged results. It is obvious from the exemplary data in Figs. 15 to 17 that hydrazine is primarily present during the first few pulses of a train and that the percentage increases with thrust level, which is as expected.

Data for two additional test conditions are shown in Fig. 18. This figure also gives an opportunity for examining the effects of initial catalyst bed temperature. These data are consistent with the data of the previous figures but are presented as ratios since hydrogen data were not available to permit calculation of mole fractions. The initial catalyst bed temperature is seen to have a major effect on the

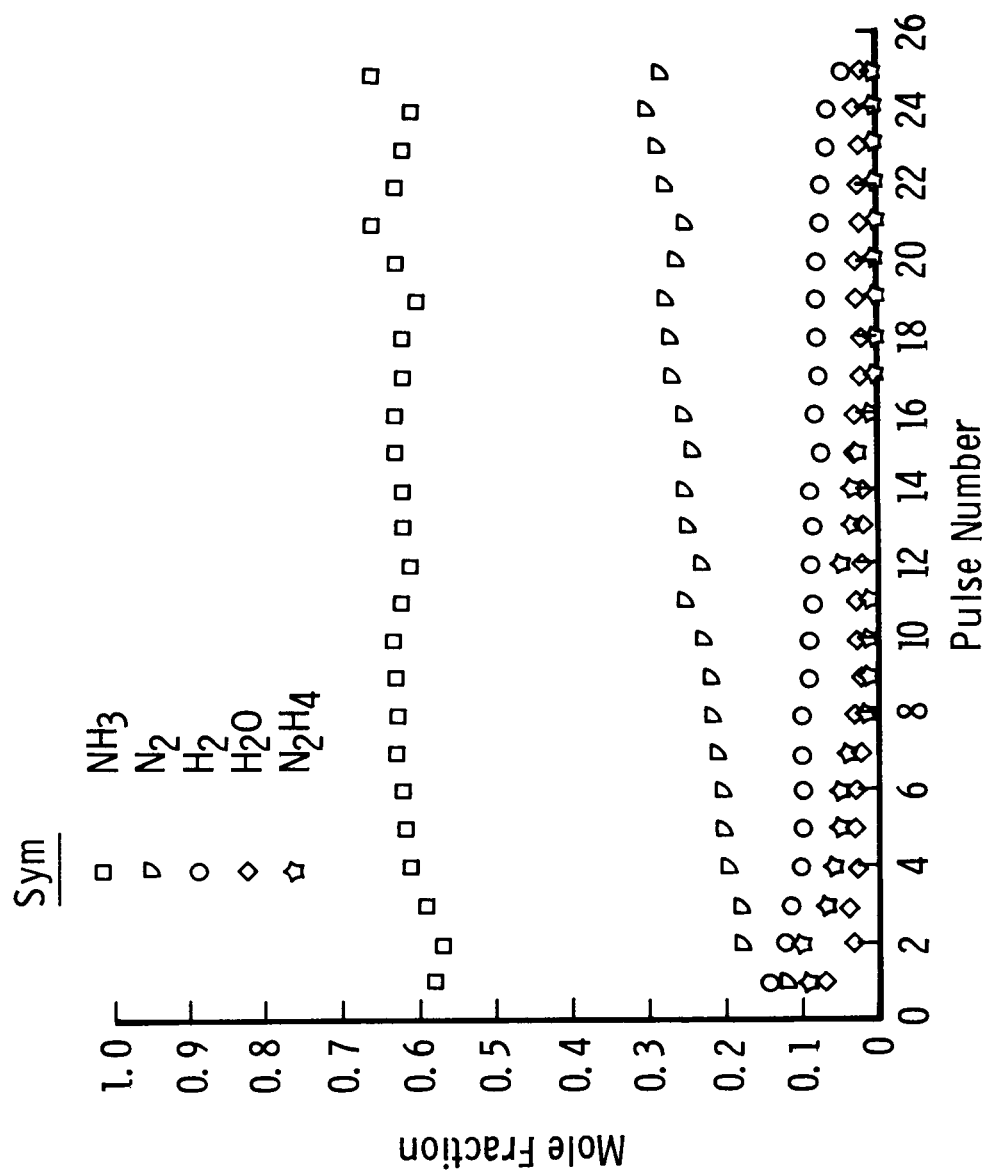


Fig. 15 Species Variation with Pulse - Condition 2A

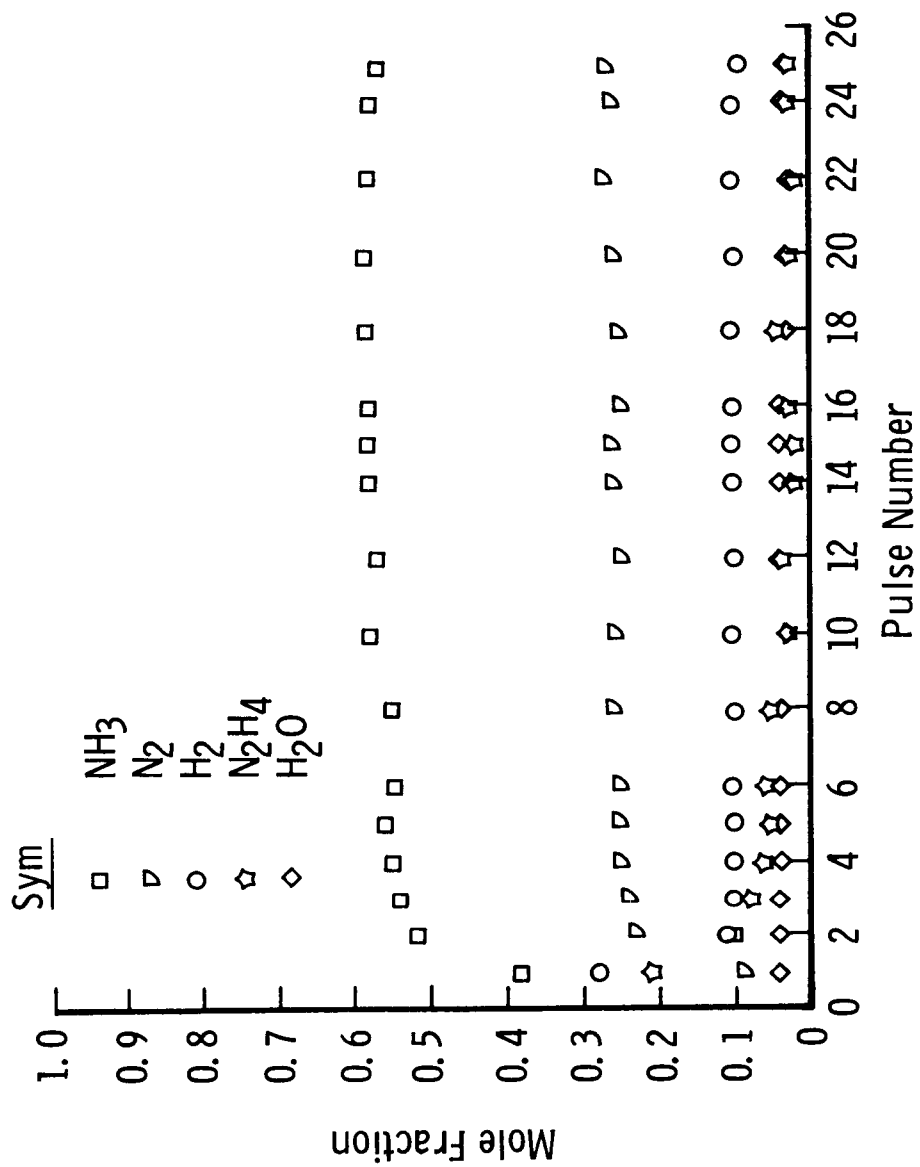


Fig. 16 Species Variation with Pulse - Condition 2B

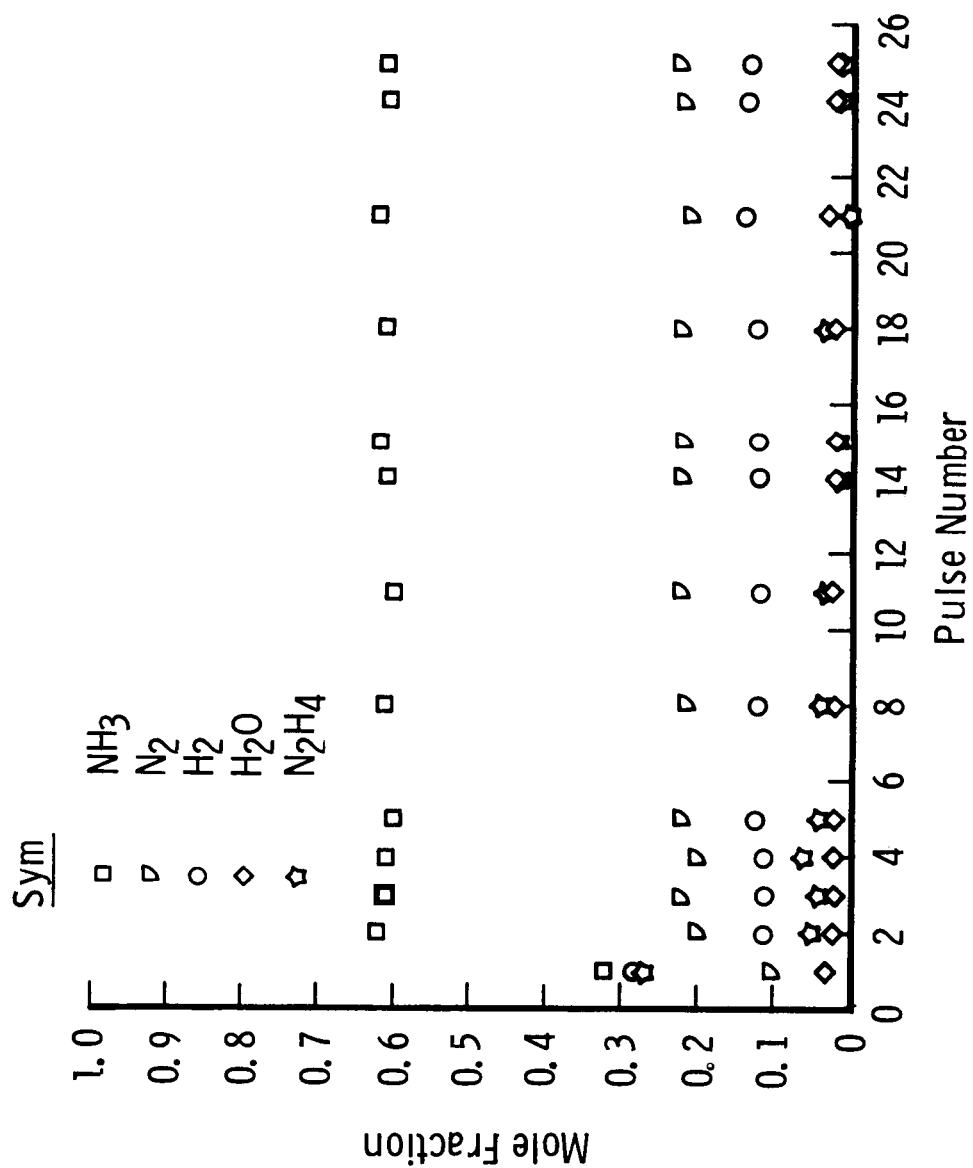


Fig. 17 Species Variation with Pulse - Condition 2C

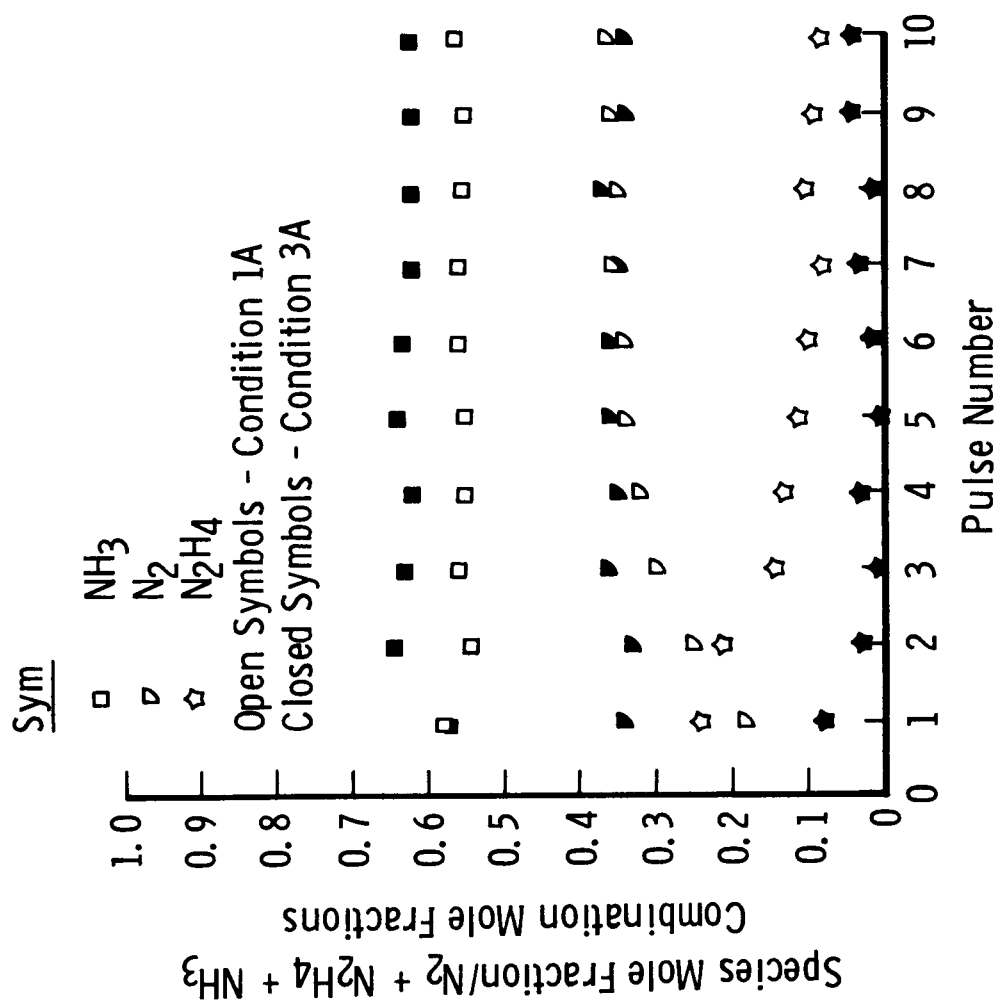


Fig. 18 Species Variation with Pulse Number

first pulse; that is, the hydrazine concentration is greatly reduced with increased temperature. After the first few pulses a consistent major difference in thruster behavior is not observed as a result of higher initial bed temperature.

### 3.2.3 Intrapulse Exhaust Species Variations

The catalyst bed temperature has been shown in the last two sections to be a very important parameter with respect to the exhaust species present in the monopropellant plume. The bed temperature varies during any particular pulse, but the engine thermocouple data do not have the time response necessary to demonstrate it. The species variation within a pulse was examined with the mass spectrometer system by sweeping over limited mass ranges so as to increase the total number of sweeps per pulse. These data were obtained primarily for test condition 2A, and examples for pulse numbers 1 and 25 are shown in Figs. 19 and 20, respectively. The data demonstrate the combination of pressure buildup and heating effects within the combustion chamber. The data are not presented in terms of mole fractions since hydrogen data were not obtained for both cases. Ratios of mole fractions of species presented may be obtained by the appropriate division of species' signals. The  $N_2H_4$  signal is seen to be very large in pulse 1 as for all other data presented previously. Note that the hydrazine concentration does decrease as the interstitial temperature increases during the remainder of the pulse. The hydrazine concentration was zero for pulse 25.

In addition to the hydrazine decrease with pulse time, the increased ammonia dissociation with the associated increases in  $N_2$  and  $H_2$  is also

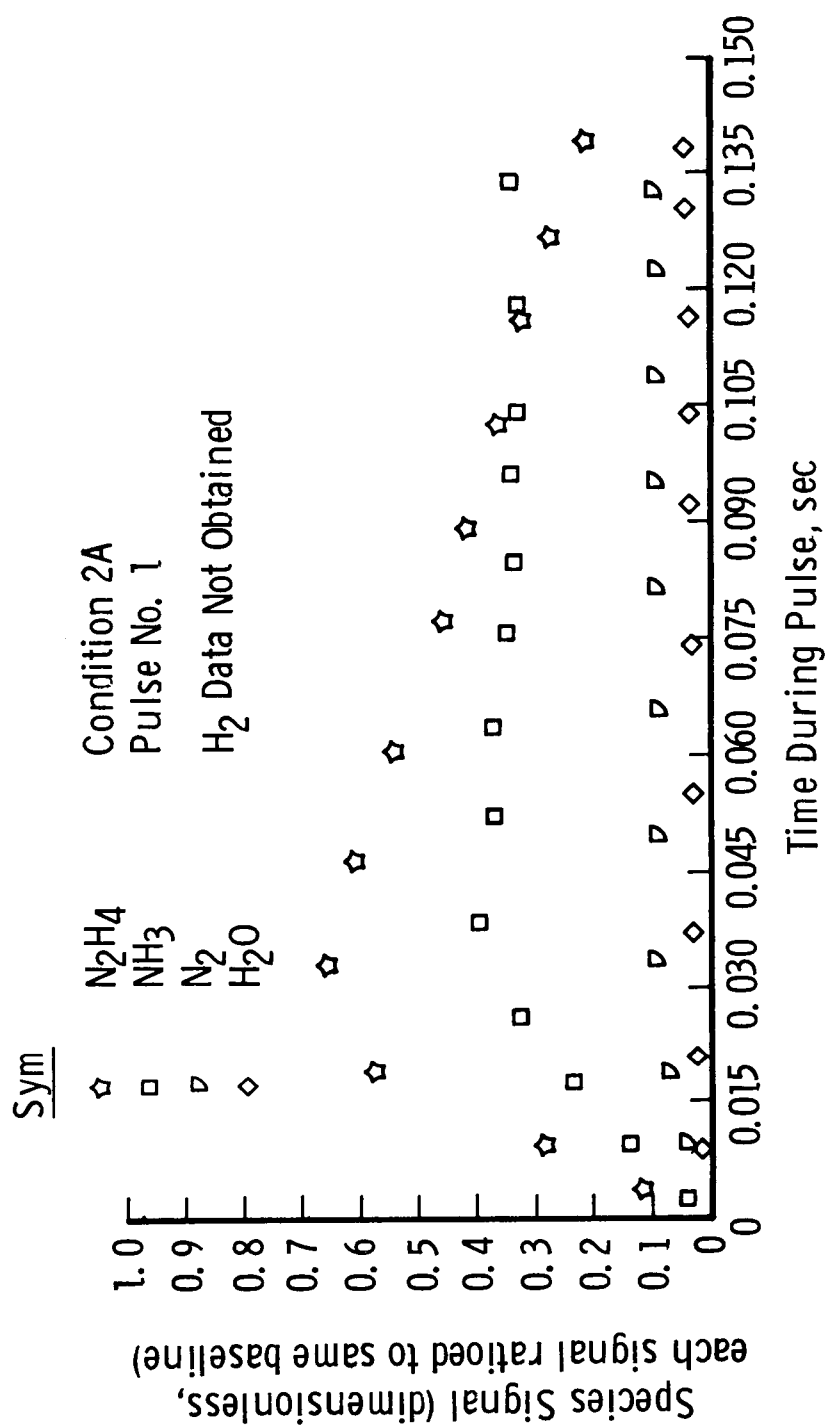


Fig. 19 Species Variation within Pulse No. 1



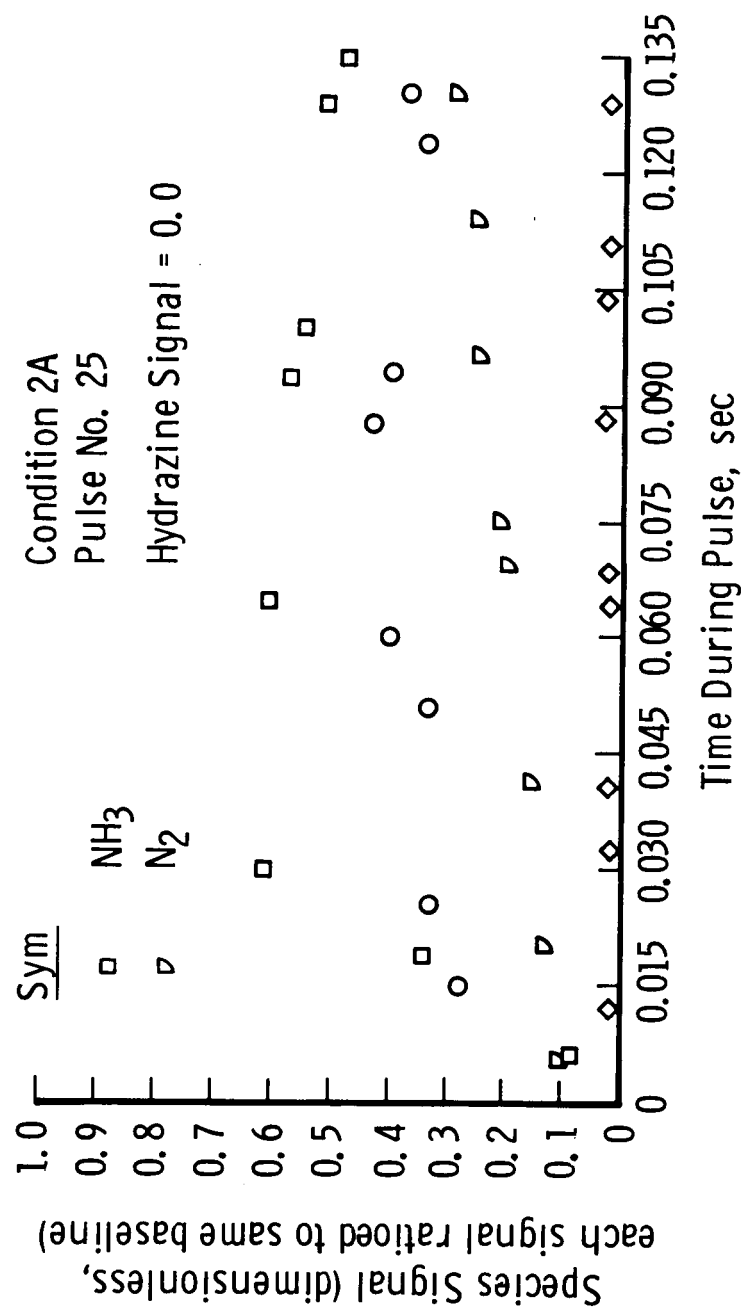


Fig. 20 Species Variation within Pulse No. 25

detectable by inspecting Figs. 19 and 20. Since a direct experimental determination of interstitial temperature was not made, no attempt at correlating the species data with temperature and pressure data was carried out.

#### 3.2.4 Pressure Dependence of Plume Hydrazine

Since the amount of hydrazine in the plume was of significant interest, a calibration sequence was run in which the amount of hydrazine (at 0.090 secs into the pulse) was recorded as a function of valve inlet pressure. Regardless of the inlet pressure, the hydrazine concentration was negligible after the first few pulses. For the first pulse, however, the amount of  $N_2H_4$  in the plume varied significantly with the inlet pressure (and hence thrust level). For an initial catalyst bed temperature of 478 K the relative variation of hydrazine in the plume as a function of pressure measured at the valve inlet is shown in Fig. 21. The change in slope of the apparently linear variation with inlet pressure was observed for more than the one calibration sequence shown, but no explanation is offered. Similar data for other catalyst bed temperatures were not obtained.

#### 3.3 Quartz Crystal Microbalance Results

Figure 22 shows the variation of the mass flux ( $\dot{m}$ ) detected by the QCM for a range of surface temperatures and at a single engine operating condition. The ordinate and abscissa display the deposited mass flux and thruster pulse number, respectively. The variation of  $\dot{m}$  with both  $T_{QCM}$  and thruster pulse number is obvious. Operation of the QCM at various temperatures ( $T_{QCM}$ ) enabled a qualitative characterization of the

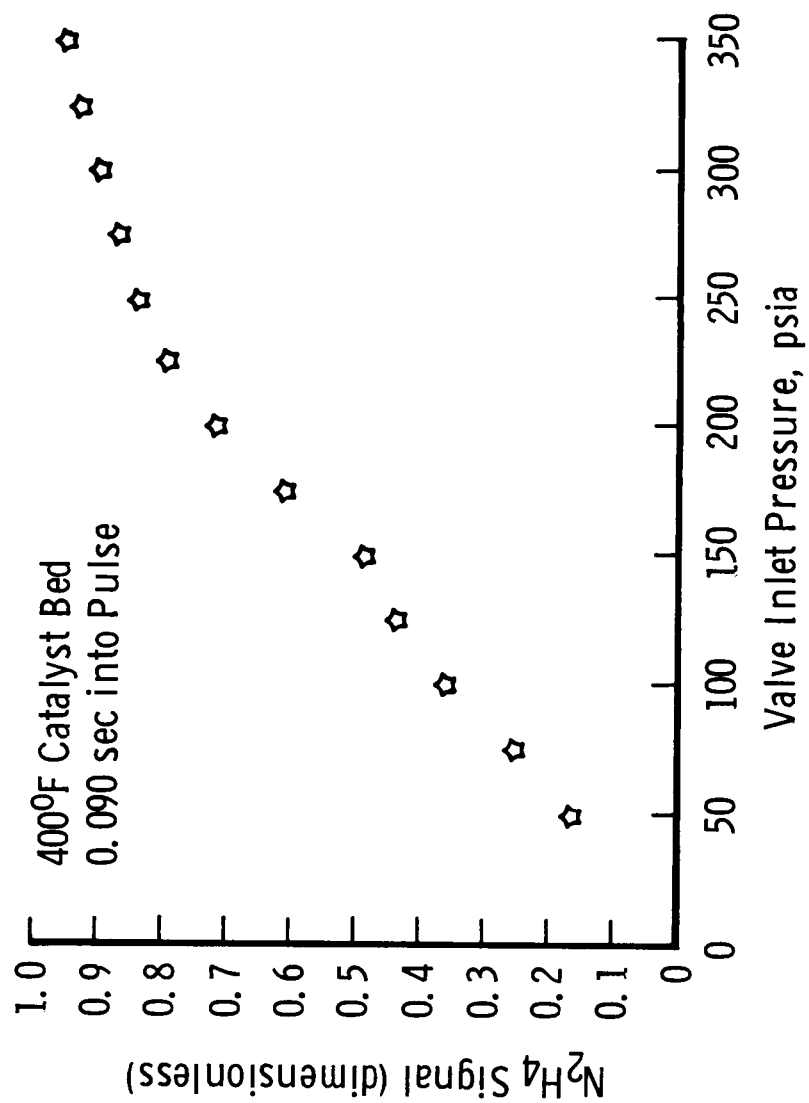


Fig. 21 Hydrazine in Plume for Pulse No. 1

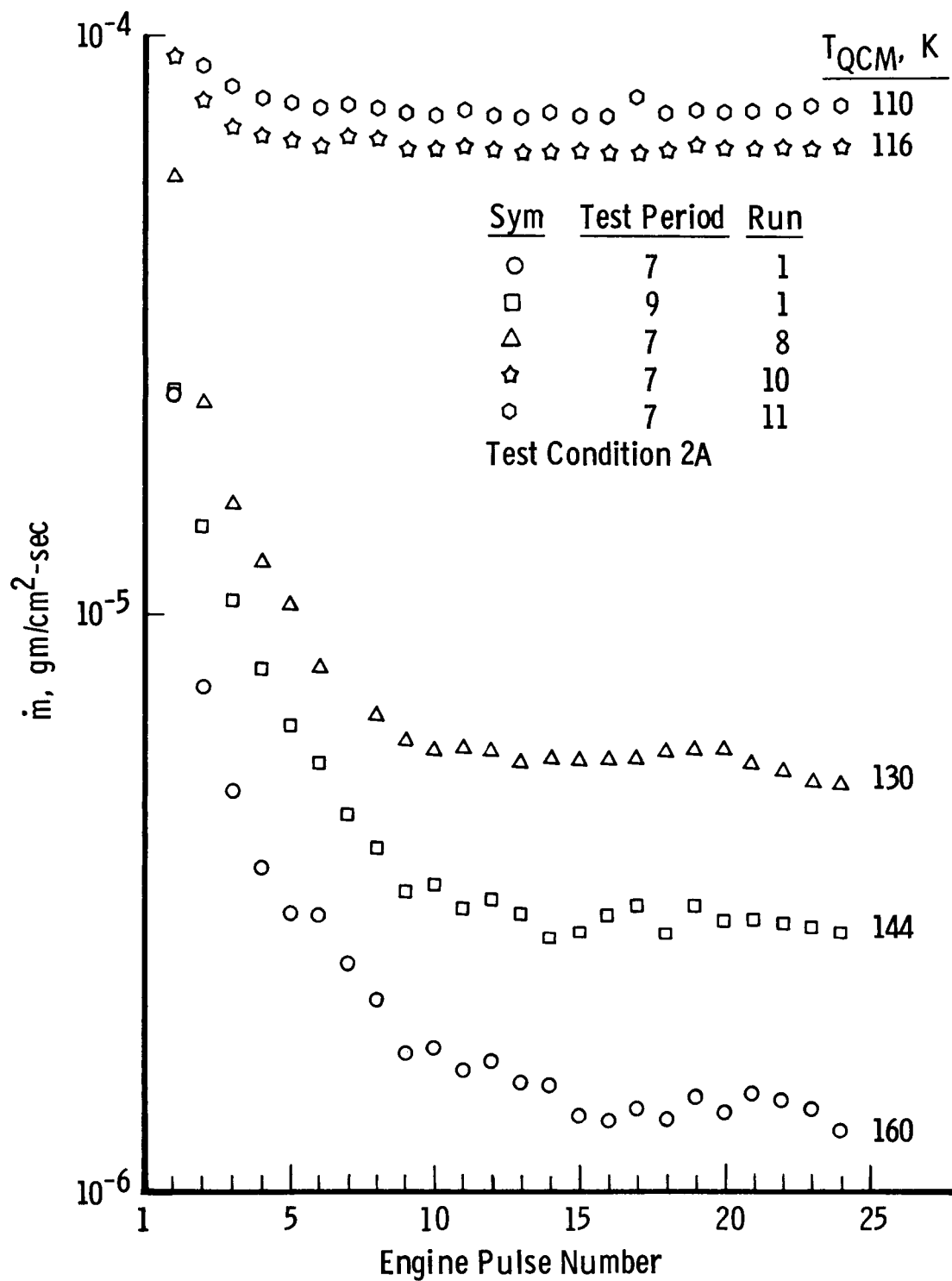


Fig. 22  $\dot{m}$  versus Pulse Number for Various QCM Temperatures

contamination species in the deposit. For  $144 \leq T_{\text{QCM}} \leq 160$  K only  $\text{N}_2\text{H}_4$ ,  $\text{H}_2\text{O}$  and trace impurities would be permanently deposited, and Fig. 22 shows such exemplary data. This variation of the contaminant mass flux with pulse number is of interest for certain operational modes of such thrusters. Although analysis of these results is still in progress, it is perhaps of interest to note that for the  $T_{\text{QCM}} = 160$  K data of Fig. 22, the cumulative mass density deposited after 20 pulses is on the order of  $70 \mu\text{g}/\text{cm}^2$  which, for an area of  $1 \text{ cm}^2$ , represents a deposit layer of thickness on the order of  $0.1 \mu\text{m}$  and would consist of approximately  $10^{17}$  molecules of, say,  $\text{N}_2\text{H}_4$ .

Further examination of Fig. 22 reveals several additional properties of the contamination. The first few pulses exhibit extremely large deposition rates for the temperature region where permanent deposition of hydrazine, water and other trace impurities is expected. After approximately ten thruster pulses, a steady-state is reached with respect to contamination deposition, and this rate is in each case nearly an order of magnitude less than that for the first thruster pulse. When the QCM surface temperature is adjusted so that in addition to the abovementioned contaminants some ammonia is permanently deposited, the main deposition rate becomes more uniform throughout the pulse train. The data clearly indicate the presence of large amounts of hydrazine, water, and other trace impurities in the first few thruster pulses with a subsequent drop to an essentially steady state. The contribution from ammonia is seen to be much greater overall and more uniform throughout the pulse train.

Figure 23 demonstrates the variation of the mass flux with engine test condition for a  $T_{\text{QCM}} = 161 \text{ K}$  at the engine axial position of 1.25 cm. Similarly, Fig. 24 depicts the variation of the average mass flux,  $\langle \dot{m} \rangle_n$ , with the engine inlet valve pressure,  $P_{\text{inlet}}$  (thrust level), for a  $T_{\text{QCM}} = 130 \text{ K}$ . Here the average of the mass flux level is performed over the last  $n = 5$  thruster pulses. The nearly two-orders-of-magnitude increase in  $\dot{m}$  with engine pulse number for a range of inlet pressures at  $T_{\text{QCM}} = 130 \text{ K}$  is presented in Fig. 25, and the large increase in  $\dot{m}$  with  $P_{\text{inlet}}$  can be viewed as a function of individual thruster pulses. Figure 25 again demonstrates large deposition rates for the first few thruster pulses at a surface temperature where hydrazine, water and other trace impurities are expected to deposit. However, the difference between this rate for the first thruster pulse and that when the thruster reaches a steady deposition rate is seen to increase dramatically with the inlet pressure. Additionally, the number of pulses required to reach the steady deposition rate is seen to increase with increasing inlet pressure.

Finally, Fig. 26 shows the variation of  $\dot{m}$  with thruster pulse number for three catalyst bed temperatures. For these data, the thruster inlet pressure was maintained at 230 psia and the surface temperature at 143 K. Here the deposition rate is seen to increase with decreasing catalyst bed temperature throughout the pulse train, with the most striking difference occurring in the first few thruster pulses. The number of pulses required to reach a steady deposition rate is also seen to decrease with increasing catalyst bed temperature.

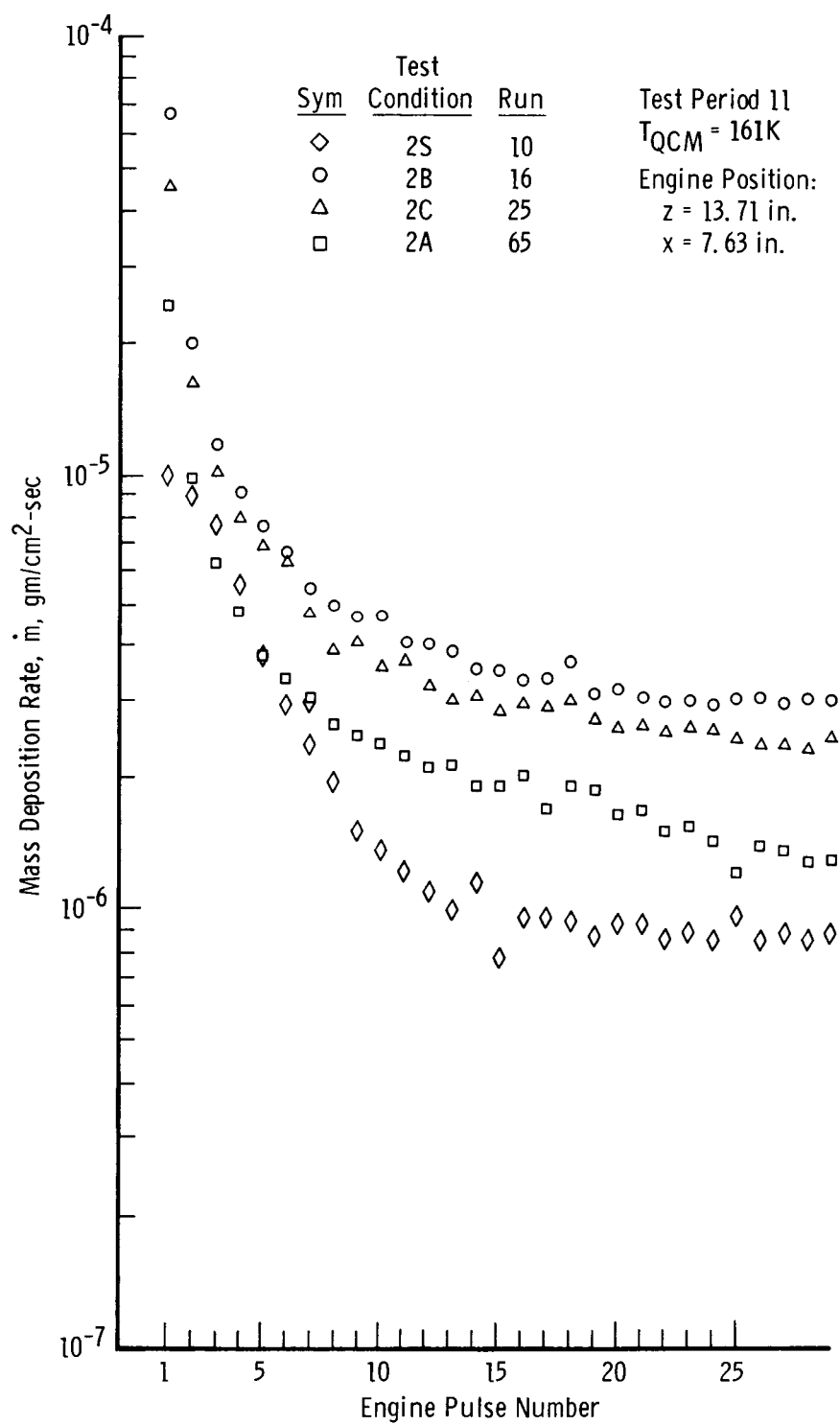


Fig. 23  $\dot{m}$  Versus Pulse Number for Several Engine Conditions

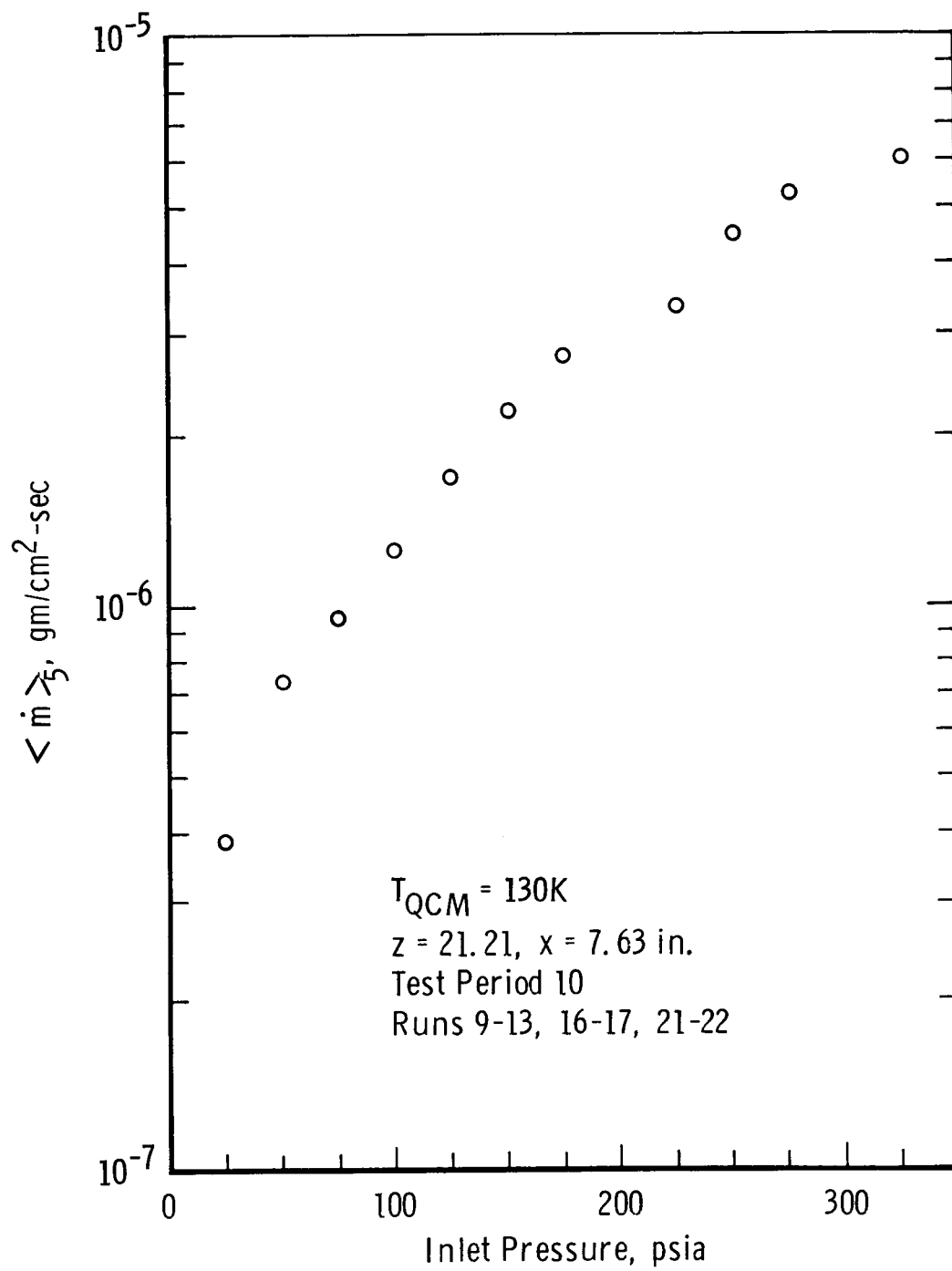


Fig. 24 Average Mass Deposition Rate versus Inlet Pressure



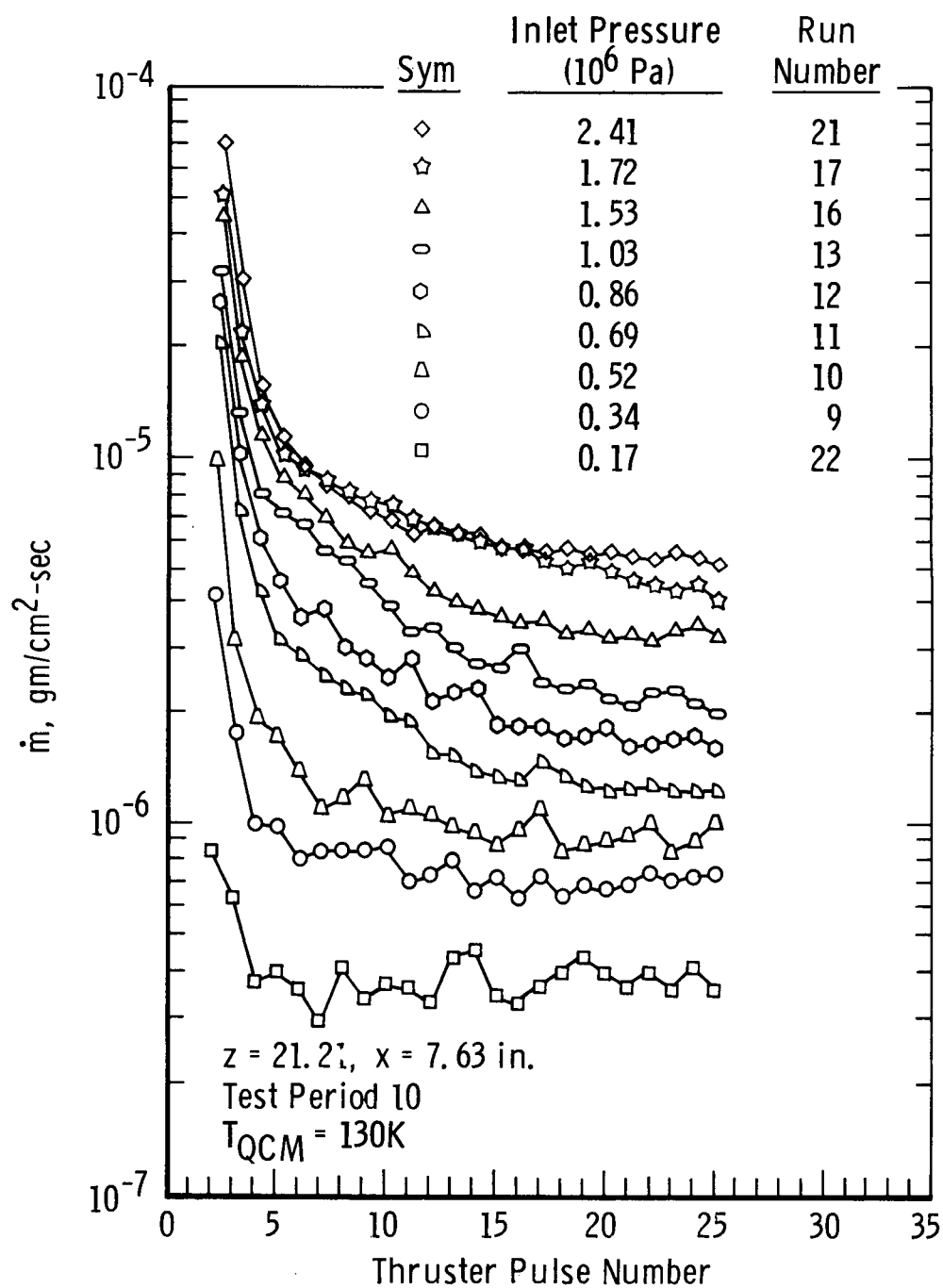


Fig. 25 QCM Mass Deposition Rate Variation with Inlet Pressure and Pulse Number

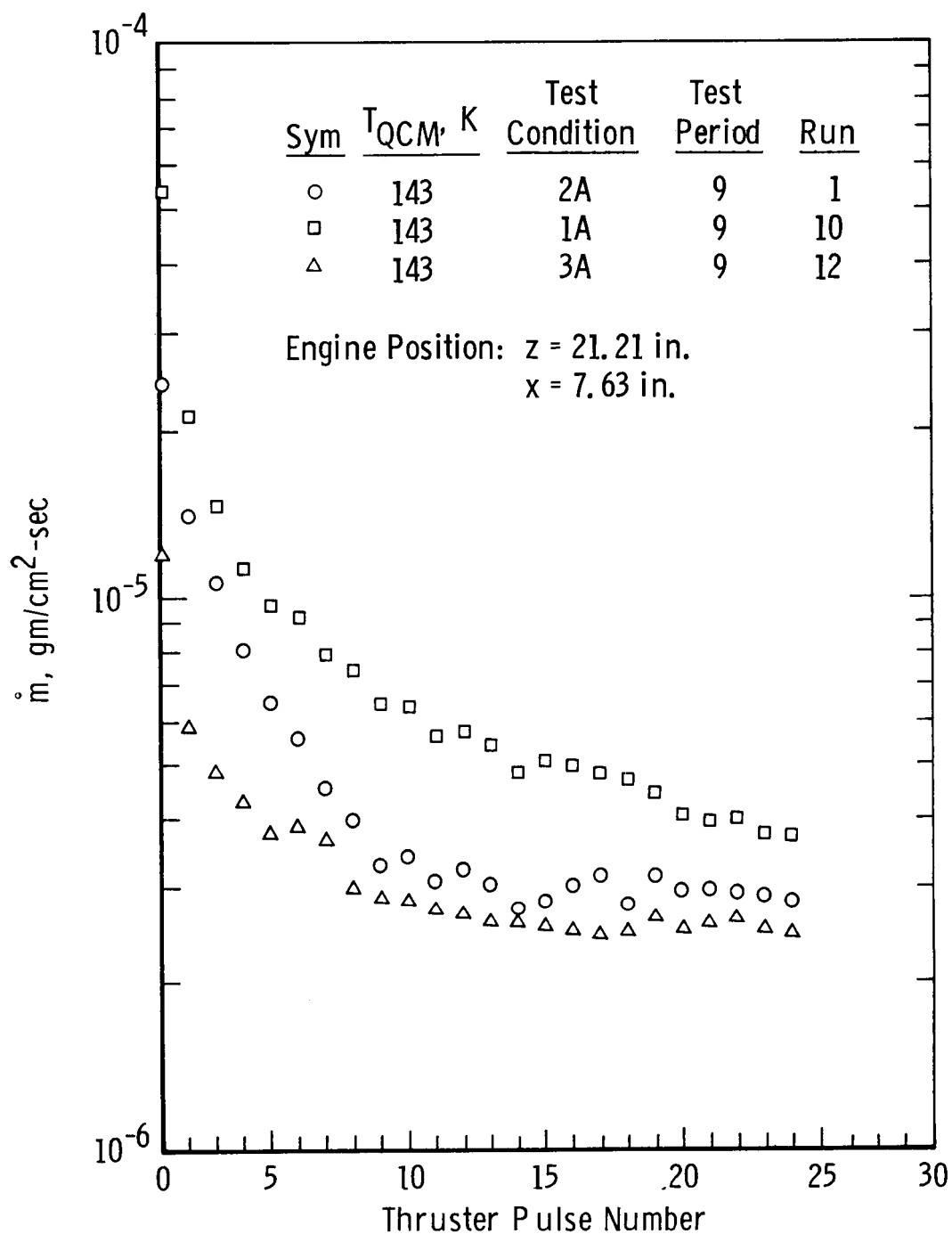


Fig. 26 QCM Mass Deposition Rate as a Function of Thruster Pulse Number

### 3.4 Catastrophic Contamination Increase

After approximately 60,000 pulses had been recorded for the engine at AEDC, in addition to 140,000 pulses previous to arriving at AEDC, a catastrophic increase in contaminant level within the exhaust was observed during test period 13. A discussion of the characterization of this occurrence is contained within this section.

#### 3.4.1 Plume Measurements.

During test period 13 the large increase in contamination levels within the plume were first observed through a dramatic increase in Rayleigh scattering. Unfortunately, the mass spectrometer had been removed to enable the installation of a centerline QCM. The QCM indicated extremely large deposition rates; so large, in fact, that saturation of the QCM occurred during the first few pulses of a train. Therefore, the web of particle collecting disks was installed in an attempt to collect and identify the contaminant species. The engine was pulsed approximately 1000 times for this collection, and the disks subsequently observed with a scanning electron microscope. The results of scanning the collected samples are discussed in the next subsection. Since the QCM had saturated for  $T_{\text{QCM}} \approx 160 \text{ K}$ , indications were that the contaminant was raw hydrazine. No Rayleigh data were obtained following this occurrence because of saturation of the photomultiplier, and no purpose was seen in attenuating the signal to obtain quantitative data. Additionally, the background, laser-induced fluorescence and/or scattering precluded further Raman measurements. Further electron beam data were acquired to determine the changes, if any, in the flowfield parameters, but analysis

of these results is still in progress.

### 3.4.2 Particle Collection

The particle collection experiment was previously described. The attempted collection of particles was successful with large quantities of submicron and larger particles captured on all three types of disks, wax, glue and copper. In addition, there was evidence of fuel droplet impingement upon the particle sampling disks. Discussions with AFRPL revealed that proof of catalyst bed particle capture required the identification of iridium among the collected particles. Extensive x-ray analysis of the collected samples failed to reveal the presence of iridium, and it was assumed that no particulate matter from the bed itself was actually collected. However, the x-ray analysis in conjunction with microscopic examination did reveal alumina spheres in large quantities. Based on the AFRPL information, these were not from the catalyst bed.

Microscopic examination of the disks did reveal that near the centerline of the plume copious quantities of liquid droplets had impinged. These droplets badly etched the pure copper surface disks, as shown in Fig. 27. A control disk obtained by spraying pure  $N_2H_4$  on a copper disk with a nebulizer revealed patterns very similar to those obtained in the plume. An example of this is shown in Fig. 28. The similarities were sufficient to establish that large quantities of hydrazine were present near the plume centerline.

The disks near the centerline were obviously subjected to high heat loads, and the collectors without wax were blackened and those with wax

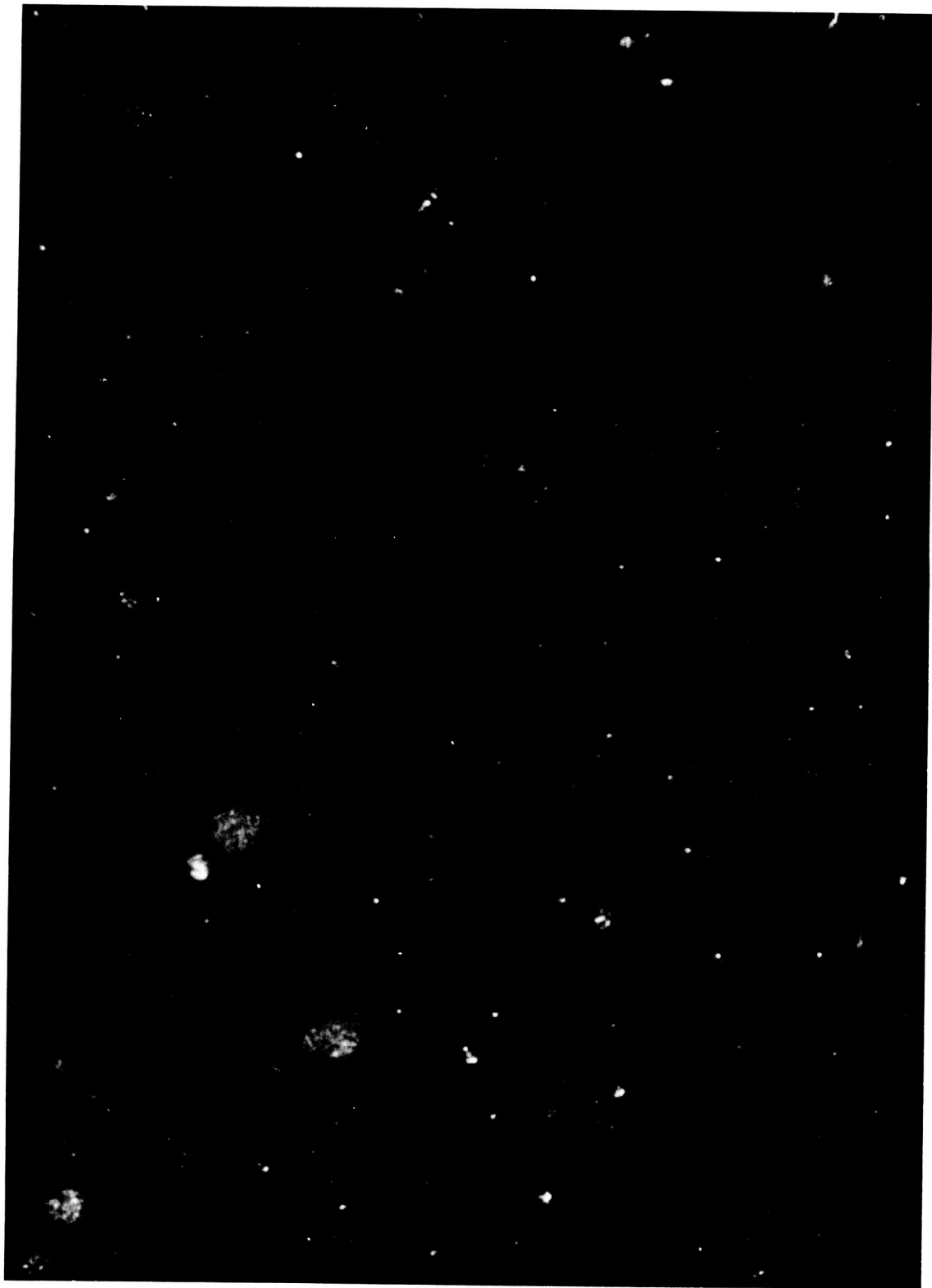


Fig. 27 SEM Sampling Disk Placed in Thruster Exhaust Plume

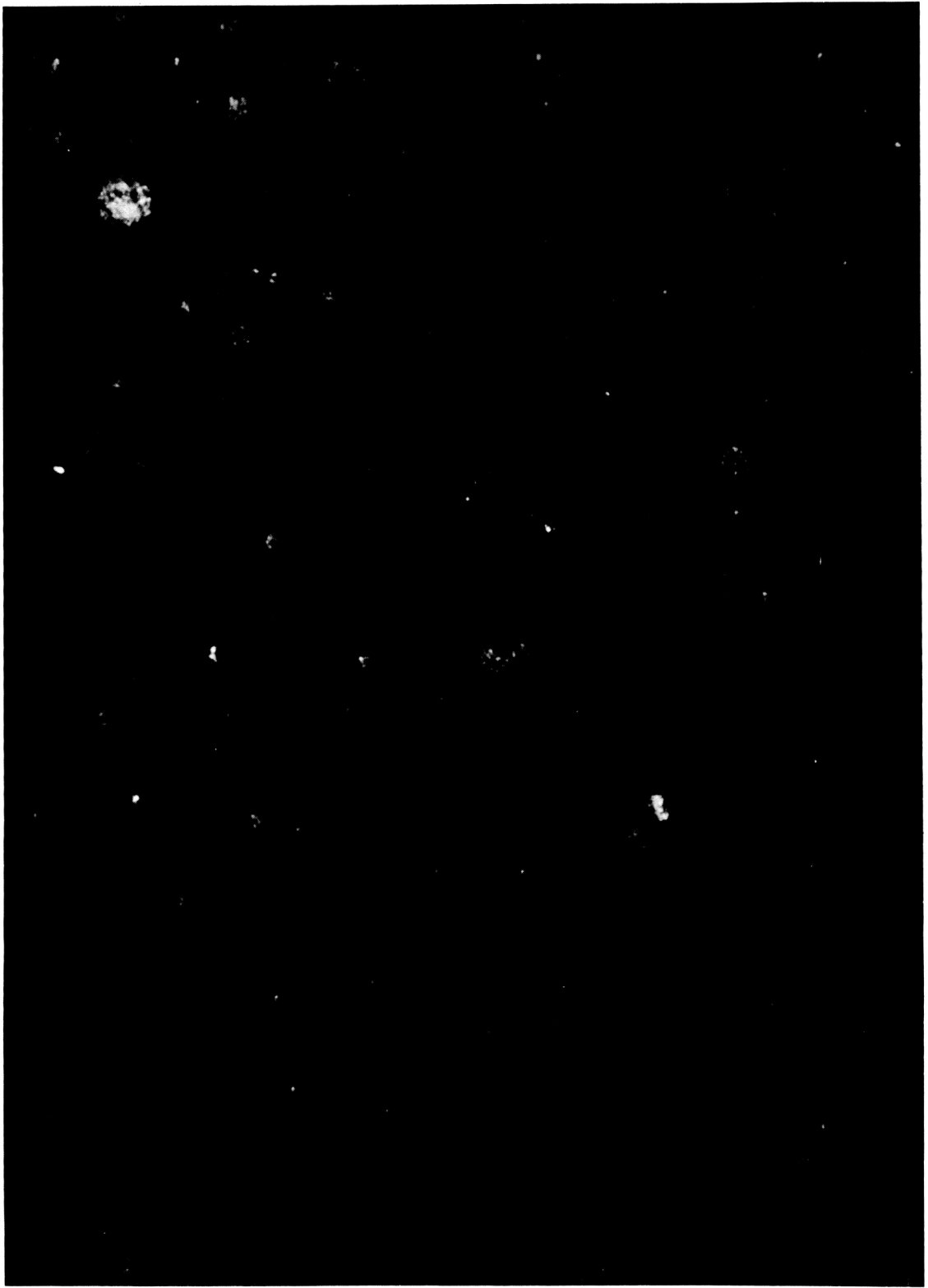


Fig. 28 SEM Sampling Disk Placed in Nebulizer Mist

were whitened. The disks just outside the direct impingement area showed the etching effects just discussed. These effects were obscured for the disks nearest the centerline because of the intense stagnation heating.

In addition to the observations reported in the preceding discussion, an interesting shadowing effect on the sampling disk mounting device was observed. This is shown in Fig. 29. The areas shielded from the plume by being behind the disks are very dark. The surfaces that appear dark but were underneath disks were noted to correspond to disks which were not pressed flat against the mounting device. A good explanation of the shadowing has not been devised at the present.

#### 3.4.3 Engine Performance

Following the observation of the catastrophic increase in exhaust contamination levels, the performance degradation of the thruster was investigated by repeating the calibration experiments conducted at the beginning of and during the research work. It could not be investigated simultaneous to the other measurements since proper operation of the thruster dictates the combustion chamber pressure tap be plugged.

The post-catastrophe mass flow rate (measured for 60-sec firings) was found to be about 10% higher than pre-catastrophe. The combustion chamber pressure and lower wall temperature changes, before and after, are demonstrated in Figs. 30 and 31, respectively. Although both pressure and temperature were different for the early and late test periods, both were still within operating limits for the thruster. The temperature drop shown in Fig. 31 is as expected for poor

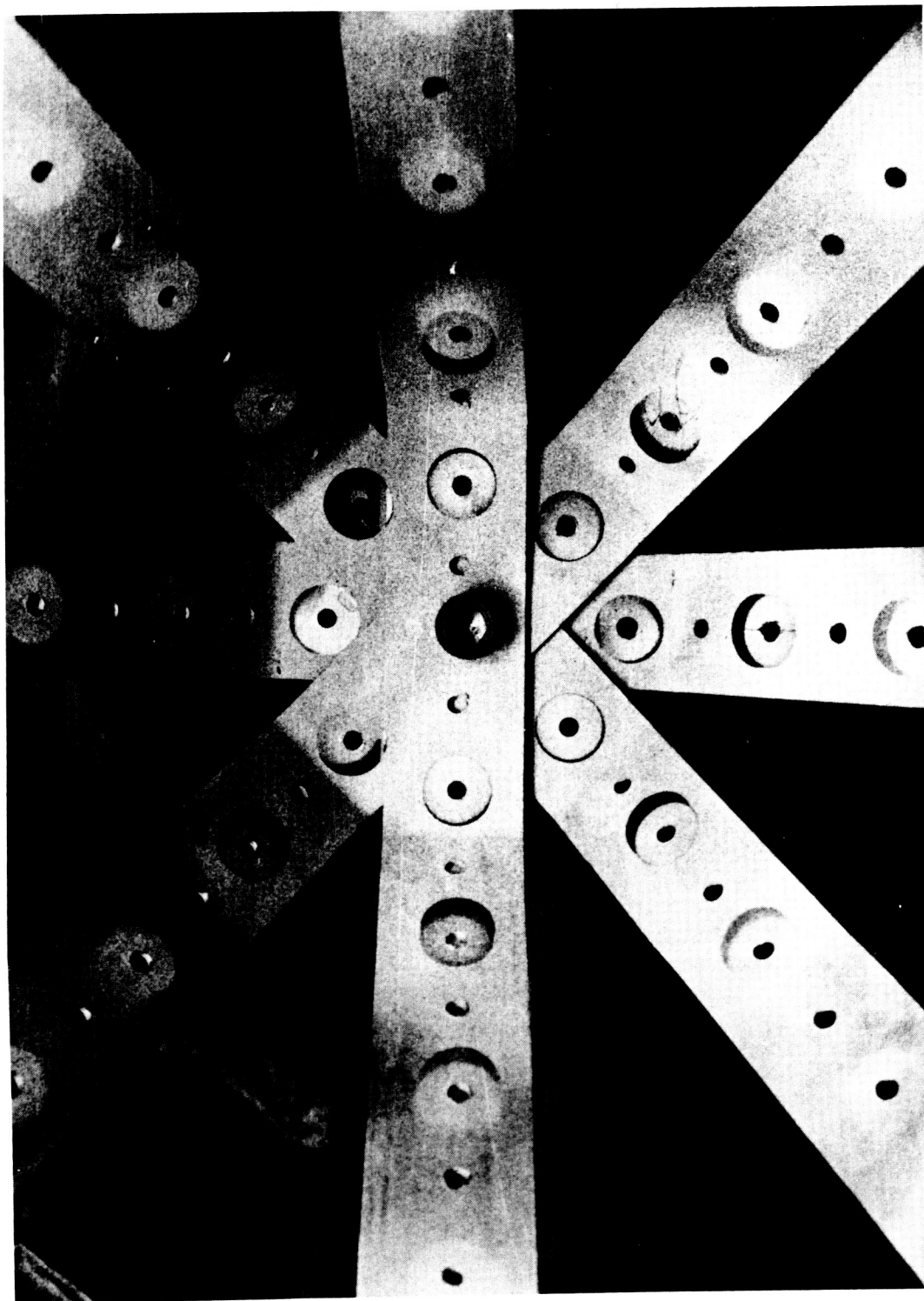


Fig. 29 Aluminum Disk Sample Holder After Testing



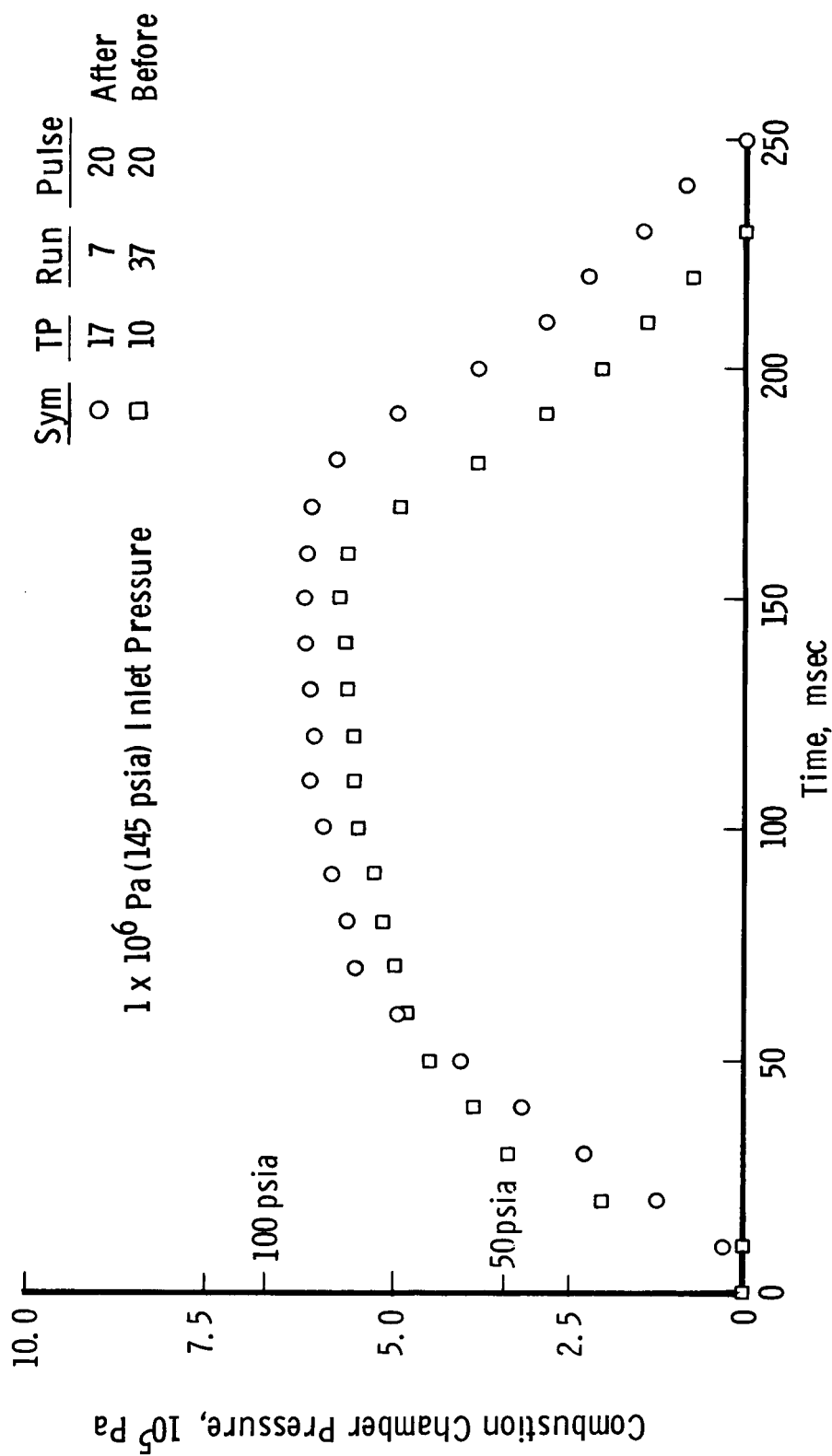


Fig. 30 Combustion Chamber Pressure Pulse before and after Increase in Contamination Level

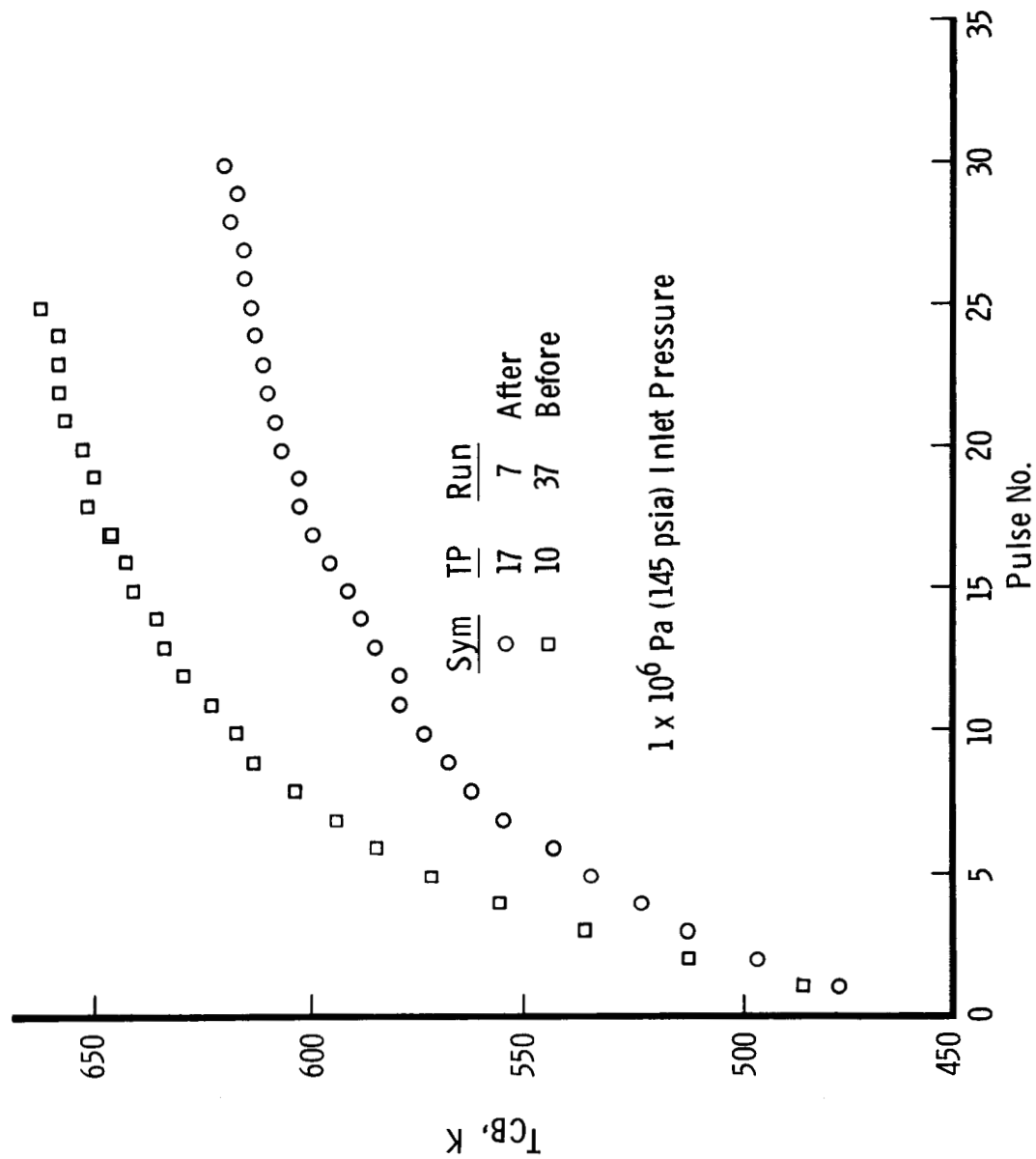


Fig. 31 TCB versus Thruster Pulse Number before and after Increase in Contamination Level

combustion, but it is interesting to note that the pressure increased as did the mass flow rate. Additional analysis of the existing data will be necessary to properly interpret engine performance, but sufficient data have been scrutinized to establish the performance to be within normally acceptable limits.

#### 4.0 CONCLUSIONS

Although the data presented here and its evaluation are preliminary, they represent the initial benefits from a detailed study of a monopropellant thruster exhaust. In addition to the information obtained concerning the engine itself, it was clearly established that the non-interfering plume measurement techniques employed in this investigation are applicable and valuable with respect to gas dynamics plume measurements. Despite the incomplete nature of the data evaluations, the following important conclusions concerning this work can be drawn:

1. The use of predictive techniques which lack nozzle-plume chemistry (also nozzle boundary layer) will be insufficient for contaminant predictions from monopropellant engines. The characteristics of thruster aging have yet to be modeled into a usable code.
2. The laser Raman-Rayleigh, electron beam fluorescence, QCM, and mass spectrometer are viable measurement systems for small engine plume measurements. Due to the indirect manner in which plume properties are obtained with the QCM, it is the least effective quantitative instrumentation implement. The data base obtainable with these systems is directly applicable to interpreting engine behavior and contamination production.

3. There are large quantities of hydrazine in the forward flow exhaust region for all operating conditions during the first few pulses of a pulse train from an aged thruster,
4. Condensate levels within the exhaust plume are high for certain engine operating conditions.
5. Copious quantities of hydrazine may be present in the forward flow region without a serious degradation or washout of the thruster occurring.

The following recommendations are obvious extensions of this work;

1. Conduct a similar investigation for the same type thruster with an unaged catalyst bed.
2. Investigate other thruster designs in similar fashion to determine if aging phenomena are consistent for such designs.
3. With the soon-to-be-established data base, evaluate in detail the present predictive capabilities, establish the discrepancies and make improvements.

#### NOMENCLATURE

$\dot{m}$	mass deposition rate on QCM surface
MOCS	method of characteristics solution
$n$	species number density
$(n/n_o)_{\text{eff}}$	effective number density ratio determined from Rayleigh/Mie scattering
$n_T, n_o$	plume total species number density and reservoir total number density, respectively
$P_{\text{inlet}}, P_c$	engine inlet pressure and combustion chamber pressure, respectively

QCM	quartz crystal microbalance
$\hat{r}$	ratio of radial distance from axial centerline to nozzle throat diameter
$T_R, T_O$	rotational temperature and reservoir temperature, respectively
$T_{CB}, T_{QCM}$	catalyst bed and QCM temperature, respectively
TC, TP	test condition and test period, respectively
$\hat{x}$	ratio of axial distance from nozzle throat to the nozzle throat diameter
$\gamma$	ratio of specific heats

#### ACKNOWLEDGMENT

This work was sponsored by the Air Force Rocket Propulsion Laboratory (AFRPL) and performed by the Arnold Engineering Development Center (AEDC), Air Force Systems Command (AFSC). Work and analysis were done by personnel of ARO, Inc., a Sverdrup Corporation company, operating contractor of AEDC.

#### REFERENCES

1. Baerwald, R. K. and Passamaneck, R. S., Monopropellant Thruster Exhaust Plume Contamination Measurements, AFRPL-TR-77-44 (1977)
2. Williams, W. D., McCay, T. D., Powell, H. M., Weaver, D. P., Price, L. L. and Lewis, J. W. L., Experimental Study of Monopropellant Hydrazine Thruster Exhaust. Paper presented at JANNAF 10th Plume Technology Meeting, San Diego, CA. (1977).
3. McCay, T. D., Powell, H. M. and Busby, M. R., Direct Mass Spectrometric Measurements in a Highly Expanded Rocket Exhaust Plume, AIAA Paper 77-154 (1977).

4. McCay, T. D., Powell, H. M. and Busby, M. R., Development of a Cryogenically Pumped Mass Spectrometer Probe for Rocket Plume Studies, AEDC-TR-76-55, June 1976.
5. Cornu, A. and Massot, R., Compilation of Mass Spectral Data, 2nd ed., Vol. I, Heydon, New York (1975).
6. Lewis, J. W. L. and Williams, W. D., Measurement of Temperature and Number Density in Hypersonic Flow Fields Using Laser Raman Spectroscopy, AIAA Paper No. 75-175, presented at the 13th AIAA Aerospace Sciences Meeting, Pasadena, CA, Jan. 20-22, 1975.
7. Lewis, J. W. L. and Williams, W. D. Argon Condensation in Free-Jet Expansions, AEDC-TR-74-32, July 1974.
8. Williams, W. D., Hornkohl, J. O. and Lewis, J. W. L., Electron Beam Probe for a Low Density Hypersonic Wind Tunnel, AEDC-TR-71-61, July 1971.